

# REPORT DOCUMENTATION PAGE

Form Approved  
OMB NO. 0704-0188

Public Reporting burden for this collection of information is estimated to average 1 hour per response, including the time for reviewing instructions, searching existing data sources, gathering and maintaining the data needed, and completing and reviewing the collection of information. Send comment regarding this burden estimates or any other aspect of this collection of information, including suggestions for reducing this burden, to Washington Headquarters Services, Directorate for information Operations and Reports, 1215 Jefferson Davis Highway, Suite 1204, Arlington, VA 22202-4302, and to the Office of Management and Budget, Paperwork Reduction Project (0704-0188), Washington, DC 20503.

1. AGENCY USE ONLY (Leave Blank)		2. REPORT DATE 29 September 2003		3. REPORT TYPE AND DATES COVERED Final Progress Report 01 Apr 01 - 30 Jun 03 <del>1 Nov 2000 - 30 Jun 2003</del>	
4. TITLE AND SUBTITLE Advanced Control Techniques for Control of Rotorcraft Vibration				5. FUNDING NUMBERS DAAD19-01-1-0390	
6. AUTHOR(S) Steven R. Hall					
7. PERFORMING ORGANIZATION NAME(S) AND ADDRESS(ES) Massachusetts Institute of Technology 77 Massachusetts Avenue Cambridge, MA 02139				8. PERFORMING ORGANIZATION REPORT NUMBER	
9. SPONSORING / MONITORING AGENCY NAME(S) AND ADDRESS(ES)  U. S. Army Research Office P.O. Box 12211 Research Triangle Park, NC 27709-2211				10. SPONSORING / MONITORING AGENCY REPORT NUMBER  42454-EG • 2	
11. SUPPLEMENTARY NOTES The views, opinions and/or findings contained in this report are those of the author(s) and should not be construed as an official Department of the Army position, policy or decision, unless so designated by other documentation.					
12 a. DISTRIBUTION / AVAILABILITY STATEMENT  Approved for public release; distribution unlimited.				12 b. DISTRIBUTION CODE	
13. ABSTRACT (Maximum 200 words)  The goal of this project is to develop vibration and control approaches and software suitable for use in the flight tests of the MD-900 helicopter, and to assist Boeing in the preparations for flight test, to enable them to use our advanced control approaches. During this effort, we have studied the feasibility of improving the robustness of X-frame actuator systems using feedback control approaches. We have investigated various feedback control design techniques to find out whether it is feasible to make the actuator robust without sacrificing its performance, and concluded that the flap position control may not be required, and even more, may be counter-productive. We have also improved the system identification methodology to investigate periodic effects, and applied it to the flight test data at Langley. Our analysis of the Langley data shows that periodic effects are negligible, so that periodic control methods are probably not required for vibration control of active rotors. Finally, we have evaluated our advanced continuous-time control system approach to reduce the helicopter vibration using wind tunnel test data at Langley, and found that our approach yields more than 20 dB of vibration reduction at the frequency components of interest.					
14. SUBJECT TERMS  Smart materials, smart structure, active rotor control, higher harmonic control				15. NUMBER OF PAGES  40	
				16. PRICE CODE	
17. SECURITY CLASSIFICATION OR REPORT UNCLASSIFIED	18. SECURITY CLASSIFICATION ON THIS PAGE UNCLASSIFIED	19. SECURITY CLASSIFICATION OF ABSTRACT UNCLASSIFIED	20. LIMITATION OF ABSTRACT  UL		

NSN 7540-01-280-5500

Standard Form 298 (Rev.2-89)  
Prescribed by ANSI Std. Z39-18  
298-102

# **Advanced Control Techniques for Control of Rotorcraft Vibration**

## **Final Report**

Steven R. Hall  
Kyungyeol Song

Massachusetts Institute of Technology  
Department of Aeronautics and Astronautics

September 29, 2003

Submitted to:

Dr. Gary Anderson  
Army Research Office  
Research Triangle Park, NC 22709-2211

Grant number: DAAD19-01-1-0390  
11/1/2000 – 6/30/2003

## Table of Illustrations and Tables

Figure 1: Transfer functions of the X-frame actuator with a high-gain amplifier.....	10
Figure 2: Frequency response of the first controller (a) and its loop transfer function (b).....	12
Figure 3: Closed-loop transfer function of the first plant obtained using the first controller. ....	12
Figure 4: Closed-loop transfer function of the second plant obtained using the first controller.....	12
Figure 5: Frequency response of the second controller (a) and its loop transfer function (b). ....	13
Figure 6: Closed-loop transfer function of the first plant obtained using the second controller.....	13
Figure 7: Closed-loop transfer function of the second plant obtained using the second controller.....	13
Figure 8: Measured and identified transfer function of the actuator.....	14
Figure 9: Frequency response of the third controller (a) and its loop transfer function (b).....	15
Figure 10: Closed-loop transfer function of the first plant obtained using the third controller. ....	15
Figure 11: Closed-loop transfer function of the second plant obtained using the third controller. ....	15
Figure 12: LTP system model with three transfer functions. ....	19
Figure 13: (a) Structure of $\Phi_{UUs}$ . (b) Structure of $\Phi_{uy}$ . ....	23
Figure 14: Input signals initiated at appropriate time intervals over the system periods. ....	24
Figure 15: Frequency responses of the lossy Mathieu equation. ....	28
Figure 16: Simulated input signals and corresponding response of the Mathieu equation. ....	29
Figure 17: Estimated harmonic transfer functions of the Mathieu equation system obtained using (a) the first method, (b) the second method. Solid and dotted line corresponds to analytical and empirical response, respectively.....	30
Figure 18: Simulated input signals and corresponding response of the Mathieu equation. The output is corrupted by white noise. ....	31
Figure 19: Harmonic transfer functions of the Mathieu equation system obtained using the first method with various $\alpha$ . (a) $\alpha=1$ , (b) $\alpha=10^7$ , (c) $\alpha=10^8$ , (d) $\alpha=10^9$ . ....	31
Figure 20: Harmonic transfer functions of the Mathieu equation system obtained using the second method. (a) Equation 40 (without smoothing technique). (b) Equation 43 (with the first smoothing technique). (c) Equation 44 (with the first and second smoothing techniques). ....	32
Figure 21: Input signal intentionally designed faulty, and corresponding response of the Mathieu equation. Both input and output signal are corrupted with noise. ....	33
Figure 22: Harmonic transfer functions of the Mathieu equation system obtained using the first method with various $\alpha$ . (a) $\alpha=1$ , (b) $\alpha=10^7$ , (c) $\alpha=10^8$ , (d) $\alpha=10^9$ . ....	33
Figure 23: Harmonic transfer functions of the Mathieu equation system obtained using the second method. (a) Equation 40 (without smoothing technique). (b) Equation 43 (with the first smoothing technique). (c) Equation 44 (with the first and second smoothing techniques). ....	34
Figure 24: ATR system mounted on the ARES helicopter testbed with in the TDT. ....	34
Figure 25: Designed input signal and corresponding response of the ATR system.....	35
Figure 26: Harmonic transfer functions of the ATR system obtained using the first method with various $\alpha$ . (a) $\alpha=10^6$ , (b) $\alpha=10^9$ , (c) $\alpha=10^{12}$ , (d) $\alpha=10^{15}$ . ....	36
Figure 27: Harmonic transfer functions of the ATR system obtained using the second method. (a) Without smoothing procedure. (b) With smoothing procedure.....	37
Figure 28: Harmonic transfer functions of the ATR system. (a) Collective, (b) Cosine cyclic, (c) Sine cyclic. ....	37
Figure 29: Effect of advance ratio on the HTFs of the ATR system. (a) Collective, (b) Cosine cyclic, (c) Sine cyclic.....	38
Figure 30: Typical open & closed-loop spectra of the hub normal shear vibratory load. ....	39
Table 1: Results of vibration reduction for ATR system (cited from [5]).....	40

## 1. Statement of Problem Studied

For more than six years, Boeing Helicopters and MIT have been working to develop actuators for helicopter rotor control that can significantly reduce the vibration typically experienced by helicopters. This work has led to the development of the X-frame actuator, which has demonstrated the bandwidth, force, and stroke required for this application. Boeing's plan was to build an actively controlled rotor with the X-frame for an MD-900 helicopter, and flight-test the active rotor system in 2002, as part of the Smart Materials and Structures Demonstration Program. The original goal of this project was to develop control approaches and software suitable for use in the flight tests of the MD-900 helicopter, and to assist Boeing before and during the flight test, to enable them to use our advanced control approaches. Our original statement of work called for us to complete the development of a system identification methodology to allow identification of the transfer function of the rotor, including periodic effects; write Matlab and/or Simulink software to implement the system identification methodology and continuous-time controller, in support of Boeing's flight test program in the DARPA Smart Structures and Materials Demonstration Program; participate in the flight test program, by analyzing data as it becomes available, and making recommendations to the flight test team. We would then, based on the flight test data, design a continuous-time control law for flight test. In addition, we would evaluate the performance of the continuous-time controller, as compared to the conventional controllers implemented, and support Boeing Mesa as needed in their design, manufacture, and analysis of the "double X-frame actuator," previously developed at MIT.

Due to delays in the flight test program, our statement of work was modified just prior to January 2003. The modification called for us to complete the analysis of the flight test data at Langley on a model, active-twist rotor, done jointly with Prof. Carlos Cesnik at the University of Michigan; analyze the new X-Frame bench data taken at Boeing, in order to improve the design of flap position controllers; and document the results of the Langley experiment and the bench tests in archival publications. In addition, we would participate in the Boeing rotor tests if those tests occur in the time frame of the effort. (In fact, the rotor tests did not occur within the time frame of the grant.)

## 2. Summary of Important Results

In this section we briefly describe the important results of our investigation. More detail on some these results are given in the Appendices.

**Wind Tunnel Test at Langley.** While Boeing prepared for the flight test, we collaborated with Prof. Carlos Cesnik's research group at University of Michigan to support his NASA-supported program for the Active Twist Rotor (ATR) in forward flight in the Transonic Dynamics Tunnel (TDT) at NASA Langley. The collaboration was carried out to test our system identification methodology and continuous-time higher harmonic control (HHC) algorithms on an actual rotor, and to gain experience for the upcoming Boeing tests. For the wind tunnel test, we implemented the system identification algorithms in Simulink to estimate the transfer function of the rotor, and designed continuous-time HHC algorithms incorporating an anti-windup scheme. Some of the important results and conclusions on the test are given below.

- We analyzed the performance of our continuous-time controllers, and found that the vibration level was significantly reduced ( $\sim 20$  dB), although we designed controllers based on the assumption that the rotor system is Linear Time-Invariant (LTI).
- We applied the system identification methodologies to investigate periodic effects in the rotor systems. The results of estimating Harmonic Transfer Function (HTF) of the rotor show that the magnitude of  $G_0$  (corresponding to LTI transfer function) is much larger than other HTF's, at least

by 20 dB. This result explains how we could achieve 20 dB of vibration reduction using continuous-time controllers based on LTI plant assumption. This is important, in that it implies that classical control laws should work well for the controlling the ATR rotor, which should greatly simplify the design of closed-loop controllers for the ATR rotor. The following section will describe the system identification methodologies in more detail.

- We developed an anti-windup system for our controller that will ensure the integrators in each loop do not wind up, and incorporated it in our continuous-time controllers during the wind tunnel tests. The results of closed-loop performance analysis show that the anti-windup system worked well as expected, and the closed-loop actuation signal was not saturated.

**System Identification Methodology.** We improved our system identification methodologies to estimate the transfer functions of a linear time periodic (LTP) system. The transfer properties of a linear time periodic (LTP) system can be described by harmonic transfer functions (HTF) that give the input-output relationship between the Fourier coefficients of the input signal and those of the output signal. The previous scheme for identifying harmonic transfer functions of LTP systems used one long input signal to speed up the transfer function estimation process, and employed a least square estimation technique to obtain HTF estimates [3]. Since this least square estimation problem is underdetermined, an additional assumption, that the transfer function is smooth, is made in the ID scheme to achieve a well-posed problem. The estimates are calculated by applying a quadratic penalty to the curvature of the transfer functions. The advantage of this approach is that we can generate an input signal quite easily to estimate the HTF's, and therefore speed up the system identification process. However, this approach requires much computer memory and intensive computation procedure, because we should take into account the power spectral density (PSD) and cross-spectral density (CSD) matrix of input and output spectrum with all frequencies simultaneously.

In contrast to the previous approach, our new approach uses  $N$  chirp signals to estimate  $N$  harmonic transfer functions. By doing that, the PSD matrix of input spectrum becomes full rank, so there would be no difficulty in inverting the PSD matrix. In this method, it is very important to take into consideration the time of application of each input relative to the system period, in order to completely characterize the system behavior, due to the time-varying nature of the system dynamics during one period. Some *ad-hoc* manners should be adopted in the new approach, as in the previous one, to generate 'smooth' transfer functions. The smoothing process we adopted for the new approach is to add some small penalty to the PSD matrix of input spectrum before inverting the matrix. This smoothing process reduces the magnitudes of the HTF's a little bit, but reduces noise in the HTF's quite significantly. It should be noted that the noise in the HTF's is sometimes very significant, so it is not easy to distinguish between the HTF's with negligible magnitude but much noise, and those with much magnitude but significant variations. However, we can distinguish them easily using this *ad-hoc* manner. That is, HTF's insensitive to the small penalty are real, while those sensitive to the penalty are artifact. In contrast to the previous approach, the new approach doesn't require much computer memory or intensive computation work, because we can compute the transfer functions at each frequency independently, without considering the whole frequency response simultaneously.

Both identification schemes have been implemented in MATLAB, and partly coded in C programming language for maximum computational efficiency. These system ID methods have been validated with analytical results for a few well-known LTP systems. The validation results show excellent agreement between the identified and analytical transfer functions. We also applied both system ID methods to investigate periodic effects in the rotor systems for the ATR at NASA Langley, and concluded that the periodic effects were negligible.

**Intelligent Anti-windup Algorithm.** We implemented an anti-windup control system for the ATR wind tunnel test at NASA Langley, and showed that it prevented the closed-loop control signal from being saturated. We could easily implement an anti-windup algorithm for a single HHC, but it was not straightforward to extend the algorithm to the multiple harmonic cases. Since we may need to implement multiple harmonic controllers simultaneously to achieve the performance requirement, it is necessary that the maximum allowable control amplitude for each anti-windup (i.e., the radius of a circle for each HHC) should be determined and distributed in a reasonable way. The easiest and simplest way would be to use the maximum control amplitudes for each HHC so that they are summed to 1. For example, when there are three HHC's in the loop, some possible ratios of the maximum control amplitudes may include 0.2:0.3:0.5, 0.3:0.3:0.4, 0.2:0.4:0.4, etc. This method guarantees that the actuators are not saturated. However, it is very likely that the method will yield very conservative control input. That is, the actual control input to the actuator may be much less than the maximum allowable control amplitude. The reason is that the control signal from each HHC may be out of phase in space (e.g., cosine cyclic vs. sine cyclic signal), and therefore tend not to affect each other. The experimental results at Langley showed that even the ratio of 0.2:0.9:0.9 for 1P collective, 4P cosine cyclic and 4P sine cyclic signal didn't saturate the actuators. This fact motivates us to develop the so-called "Intelligent anti-wind algorithm" for multiple HHC's.

There may be several ways to implement anti-windup algorithms for multiple HHC's that will yield better performance, compared with the conservative method mentioned earlier. Our first intelligent anti-windup algorithm sets up the initial ratio of the maximum control amplitudes for each control loop, and increases or decreases the ratios gradually so that the control input can be maximized without saturating the actuators. This algorithm is quite simple in that the initial ratio of the maximum control amplitudes is preserved during the control operation. However, the algorithm would yield satisfactory closed-loop results if the initial ratio is reasonably selected. We are also developing methods to determine the optimal ratio of the maximum control amplitudes for each HHC in real time.

The intelligent anti-windup scheme was implemented in Simulink, and simulation results show that the technique is effective at preventing integrator windup. The Simulink tool is available for future closed-loop tests.

**Flap Position Control Loop.** One of the concerns raised by Boeing is that the actuators on different blades may have slightly different scale factors, so that the same voltage input to all the actuators may produce different flap deflections, and hence yield an unbalanced input to the rotor. As requested by Boeing, we have worked on the feasibility study of improving the robustness of X-frame actuator systems using "inner loop" position controllers to ensure that all flaps respond the same way. We investigated various feedback controllers on the open-loop frequency responses of X-frame actuator installed in the bench test rig, which were measured at Boeing in September 2002. The main result of our work is that we can achieve roughly 50% of reduction in the sensitivity of the plant to uncertainty below 40 Hz, without causing serious performance degradation above 100 Hz. If we want more reduction in the plant's sensitivity in the low frequency range, we have to accept worse performance in the high frequency range, and vice versa. Also, we can achieve quite high robustness of the plant at the harmonic frequencies using several higher harmonic controllers, as well as broadband feedback controller.

Our feasibility study shows that the inner-loop position controller reduces the sensitivity in the plant to uncertainty to some extent. However, our recommendation is that the inner-loop position controller may be counter-productive, and therefore should not be used unless it is clear that the actuator deflections are significantly different from blade to blade, because the inner-loop position controller reduces the stability margins of the outer-loop vibration control.

### 3. Papers submitted or published

We have submitted two journal papers and one conference paper to the Journal of the American Helicopter Society. A list of the papers submitted is given below.

Manuscripts submitted, but not published:

- Shin, S. J., Cesnik, C. E. S., and Hall, S. R., “Closed-loop Control Test of NASA/ARMY/MIT Active Twist Rotor System, Part I: System Identification,” submitted to *Journal of the American Helicopter Society*.
- Shin, S. J., Cesnik, C. E. S., Hall, S. R., and Song, K. Y., “Closed-loop Control Test of NASA/ARMY/MIT Active Twist Rotor System, Part II: Controller Implementation,” submitted to *Journal of the American Helicopter Society*.

Papers published in conference proceedings:

- Shin, S. J., Cesnik, C. E. S., and Hall, S. R., “Closed-loop Control Test of NASA/ARMY/MIT Active Twist Rotor for Vibration Reduction,” Presented at the American Helicopter Society 59<sup>th</sup> Annual Forum, Phoenix, Arizona, May 6-8, 2003.
- S.-J. Shin, C.E.S. Cesnik, and S.R. Hall, “Helicopter Vibration Reduction in Forward Flight Using Blade Integral Twist Control,” American Helicopter Society 58<sup>th</sup> Annual Forum, Montreal, Canada, June 11-13, 2002.

Technical reports submitted to ARO:

- Afreen Siddiqi and Steven R. Hall, “Identification of the Harmonic Transfer Functions of a Helicopter Rotor,” Report AMSL #01-01, Active Materials and Structures Laboratory, MIT, Cambridge, MA.

We are also preparing the following journal paper that will be submitted soon to the *Journal of Guidance, Control, and Dynamics*:

- Song, K., Siddiqi, A., and Hall, S. R., “Development of System Identification Methodologies for Linear Time Periodic Systems,” in preparation, *Journal of Guidance, Control, and Dynamics*.

### 4. Scientific Personnel

1. Dr. Steven R. Hall, Professor of Aeronautics and Astronautics.
2. Ms. Afreen Siddiqi, formerly a graduate student in the Department of Aeronautics and Astronautics. Earned SM degree while employed on project.
3. Dr. Kyungyeol Song. Department of Aeronautics and Astronautics.

### 5. Report of Inventions

None

## 6. Bibliography (Cited Above and in Appendices)

1. Wereley, N. M. and Hall, S. R., "Frequency Response of Linear Time Periodic Systems," *Proceedings of the 29th IEEE Conference on Decision and Control*, Honolulu, HI, December 5–7, 1990, pp. 3650–3655.
2. N. Wereley, "Analysis and Control of Linear Periodically Time Varying Systems," PhD thesis, Massachusetts Institute of Technology, Department of Aeronautics and Astronautics, February 1991.
3. Afreen Siddiqi and Steven R. Hall, "Identification of the Harmonic Transfer Functions of a Helicopter Rotor," Report AMSL #01-01, Active Materials and Structures Laboratory, MIT, Cambridge, MA.
4. Eric F. Prechtel and Steven R. Hall, "Closed-Loop Vibration Control Experiments on a Rotor With Blade Mounted Actuation," AIAA/ASME/AHS Adaptive Structures Forum, Atlanta, Georgia, 3–6 April 2000. AIAA 2000-1714.
5. Shin, S. J., Cesnik, C. E. S., and Hall, S. R., "Closed-loop Control Test of NASA/ARMY/MIT Active Twist Rotor for Vibration Reduction," Presented at the American Helicopter Society 59<sup>th</sup> Annual Forum, Phoenix, Arizona, May 6–8, 2003.



## A Flap Position Control Loop

We have worked on the feasibility study of improving the robustness of X-frame actuator systems using “inner loop” position control approaches. This work was conducted as requested by Boeing, who concerned that the actuators on different blades may have slightly different scale factors, so that the same voltage input to all the actuators may produce different flap deflections, and hence yield an unbalanced input to the rotor. We have investigated various feedback control algorithms on the open-loop frequency responses of X-frame actuator installed in the bench test rig, which were measured at Boeing in September 2002, to ensure that all flaps respond the same way. This section describes the basic concept, design procedures, simulation results, and some comments for flap position control loop.

### A.1 Basic Concept of Flap Position Control Loop

A block diagram describing the open-loop actuator system (i.e., without the flap position control loop) is shown in Figure (a).

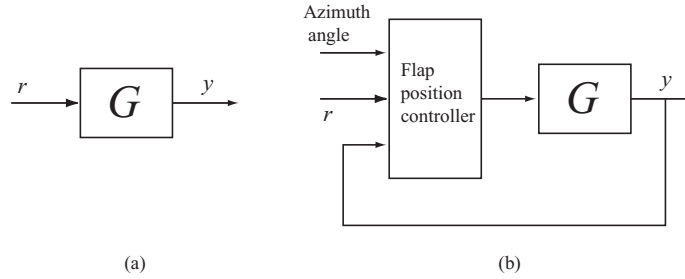


**Figure 1: Block diagram of actuator system. (a) Open-loop, (b) Closed-loop.**

Here,  $y$  is the actual actuator response,  $r$  is the command actuator input, and  $G$  is the system function (linear or nonlinear) of the actuator system. We want  $y$  to follow  $r$  (i.e.,  $y \approx r$ ), especially at the bandwidth of interest, so that the uncertainty in  $G$  does not affect the actuator response. As for the “bandwidth of interest”, we mean broadband frequency ranges below  $6P$  (i.e. between 0 and  $6P$ ), or at least several harmonic frequencies (e.g.,  $1P$ ,  $2P$ ,  $3P$ , ...) if broadband feedback control is not possible. We may also use both broadband and harmonic controllers at the same time, in order to satisfy the requirement of reducing the effect of the uncertainty on the actuator response. In any case, the block diagram of closed-loop actuator system, including the flap position control loop, can be represented as in Figure (b). Using the flap position control loop, the actuator response  $y$  is expected to follow its command input  $r$  within the bandwidth of interest, regardless of the uncertainty in  $G$ .

### A.2 Transfer Function of Actuator Systems

Before designing any controller, it is necessary to estimate the open-loop transfer function of the system and investigate their properties. Figure 1 shows the open-loop frequency responses of the X-frame actuator installed in the bench test rig, which were measured in September 2002 at Boeing. Note that the frequency responses in Figure 1 include the dynamics of high-gain amplifier. Also, note that a 2 kHz 4-pole Bessel filter, which was used during the data acquisition probably to reduce the sensor noise and aliasing effect, was replaced by a 4 kHz Butterworth filter to facilitate the design of feedback controllers.

Frequency responses in Figure 1 show some undesirable features of the actuator dynamics for controller design. First, the actuator response has a large resonance around 100 Hz, with varying frequency depending on the boundary condition, and several other resonance above 200 Hz. Recalling that the bandwidth of interest for our applications is below 40 Hz ( $\sim 6P$ ), the effects of the resonance around 100 Hz on the controller design would be significant. The effect of resonance could be reduced using a notch filter, if they do not vary considerably with frequency. However, as shown in Figure 1, the

frequency of the resonance in our actuator system changes quite significantly, which implies that a notch filter cannot be used to cancel it out. Another undesirable feature of the actuator dynamics is the substantial phase lag in the response above 300 Hz, especially in the transfer function with light color (clamp position 6). The phase lag limits seriously the magnitude of controller, and therefore the performance of closed-loop systems; the loop gain should be much less than unity above 300 Hz to avoid any instability problem, which also limits the loop gain below the bandwidth of interest ( $\sim 40$  Hz). Therefore, the actuator system we are dealing with forces us to accept a trade-off between high performance below 40 Hz (i.e., high robustness to uncertainty) and low performance above 300 Hz (i.e., high sensitivity to uncertainty).

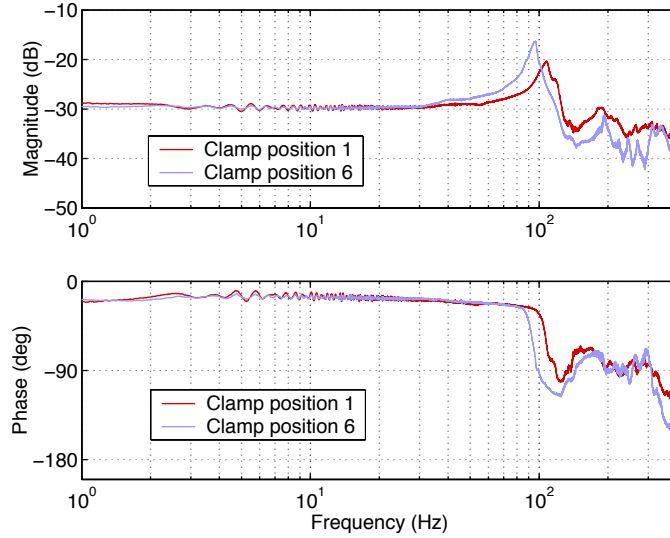


**Figure 1: Transfer functions of the X-frame actuator with a high-gain amplifier.**

### A.3 Design of Controllers and Simulation Results

In order to investigate the feasibility of applying flap position control loop, we designed various feedback controllers and compared the advantages and disadvantages of each one. Here, we present the design concept and simulation results for three controllers among them.

#### (1) The first controller: classical (non model-based) & broadband controller

In the first controller design approach, we adopted the classical control design technique (i.e., non model-based approach), aiming at achieving a ‘good loop shape’ in a broadband frequency range. Here, ‘good loop shape’ means that the loop transfer function will have as high loop gain as possible below 40 Hz, while stabilizing the closed-loop system with enough gain/phase margins. It was our belief that the loop gain should be at least 10 dB within the bandwidth of interest, in order to achieve the closed-loop system with acceptable performance (note that the loop gain of 10 dB will reduce the sensitivity of the actuator to uncertainty by about 3 times, i.e.,  $\sim 70\%$ ). However, it turned out that this level of loop gain could not be achieved without serious stability problems in the high frequency ranges, due to the undesirable dynamics described in the previous section. After some trade-off analysis between the performance within the bandwidth of interest (below 40 Hz) and stability problems in the high-frequency ranges (above 100 Hz), we concluded that the maximum loop gain we could achieve at 40 Hz using a classical approach, without compromising the gain/phase margins, is about 5 dB.

The frequency response of the first controller is shown in Figure 2(a), and the resulting loop transfer function and sensitivity transfer function for each actuator response (clamp position 1 and 6) are shown in

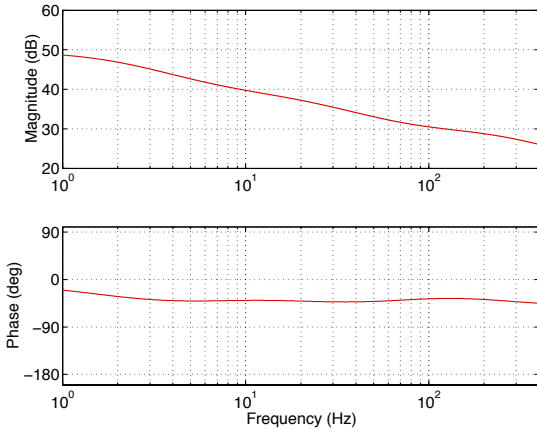
Figure 2(b). Here, the first and second plant corresponds to the transfer function with dark (clamp position 1) and light (clamp position 6) color in Figure 1, respectively. Also, note that the sensitivity transfer function provides the information about the reduction of the closed-loop actuator system's sensitivity to uncertainty, compared with its open-loop counterpart. In other words, if the magnitude of the sensitivity transfer function is  $-20$  dB, it means that the sensitivity of the actuator response to uncertainty is reduced by 20 dB (i.e., 10 times) using the feedback controller. The loop transfer functions in Figure 2(b) show that the first controller actually achieves about 6 dB of loop gain below 40 Hz, with acceptable gain and phase margins. Therefore, we can expect that the sensitivity of the closed-loop actuator system to uncertainty will be reduced by a factor of 2 below 40 Hz. The expectations are supported by the sensitivity transfer functions shown in Figure 2(b), whose magnitude is lower than  $-6$  dB below 40 Hz. As mentioned earlier, this level of performance was a result of many trade-off analyses between the performance and stability in the low- and high-frequency ranges, respectively. If we want to achieve better performance (higher loop gain) below 40 Hz, we have to accept worse stability (lower gain/phase margin) above 100 Hz.

The closed-loop transfer function for each actuator response is shown in Figure 3 and Figure 4, respectively, with both zoomed-out (a) and zoomed-in (b) versions. In order to see how robust the closed-loop actuator system is to uncertainty, the magnitude of the open-loop actuator response was increased and decreased by 30 % artificially, and the closed-loop performance of each case was compared with that of the nominal one. The results of Figure 3 and Figure 4 indicate that the variation in the magnitude of the closed-loop actuator system with uncertainty is within around 1.5 dB below 40 Hz. Considering that 30 % of uncertainty corresponds to roughly 3 dB, we can conclude that the first controller reduced the sensitivity of the actuator at least by a factor of 2 below 40 Hz.

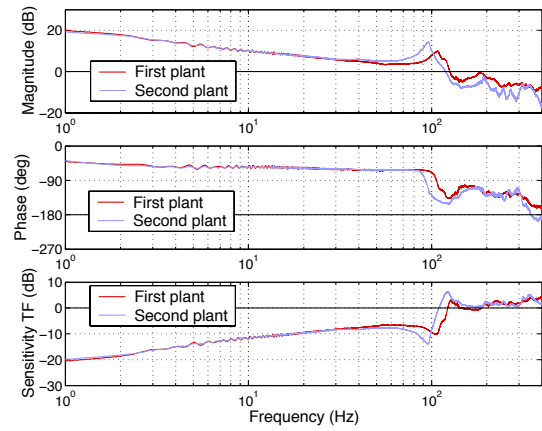
## **(2) The second controller: classical & broadband/harmonic controller**

The first controller aimed at improving the robustness of the actuator in a broadband frequency range, i.e. between 0 and 40 Hz. As described earlier, there was a limit in increasing the gain for the broadband feedback controller (and therefore, improving the performance of the closed-loop system), due to the substantial resonant peak and phase delay in the actuator response. Considering these limitations, we designed the second controller, which wraps several higher harmonic control loops around the closed-loop actuator system with the first controller. In other words, the second controller contains the first controller and several higher harmonic controllers. Using the proposed controller, the actuator response follows its command input at each harmonic frequencies 1P~6P regardless of the uncertainty in the system.

The frequency responses of the controller, the resulting loop transfer functions and sensitivity transfer functions, and the closed-loop actuator transfer functions are shown in Figure 5 – Figure 7. Basically, all of the results shown here are the same as those obtained using the first controller, except at each harmonic frequencies 1P~6P (here, 1P is assumed to be 6.5 Hz). That is, the second controller reduces the sensitivity of the actuator to uncertainty by a factor of 2 below 40 Hz except the harmonic frequencies, without making the performance above 100 Hz worse too much. At the harmonic frequencies, the loop gains are infinite, and therefore the magnitude of the sensitivity transfer function becomes zero, which implies that the uncertainty in the system or environment does not affect the actuator response at the harmonic frequencies at all. These phenomena can be observed from the closed-loop responses in Figure 6 and Figure 7.

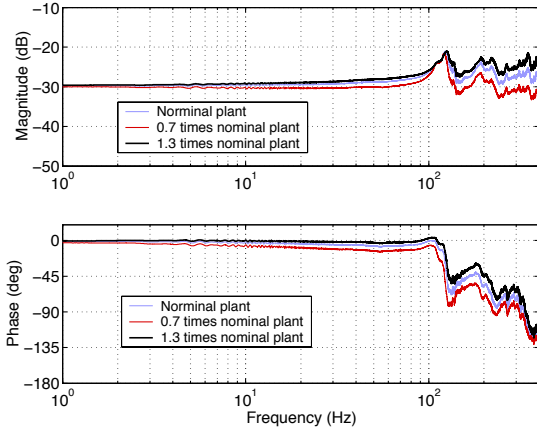


(a)

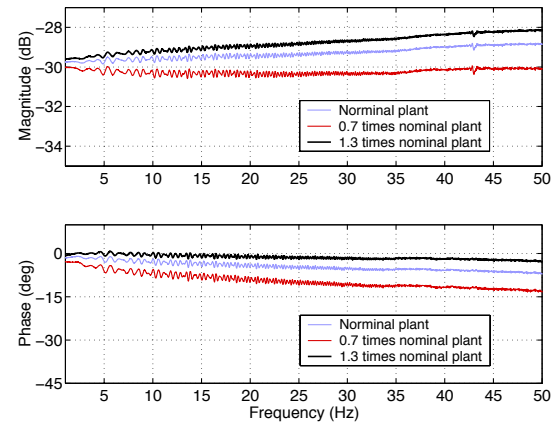


(b)

**Figure 2: Frequency response of the first controller (a) and its loop transfer function (b).**

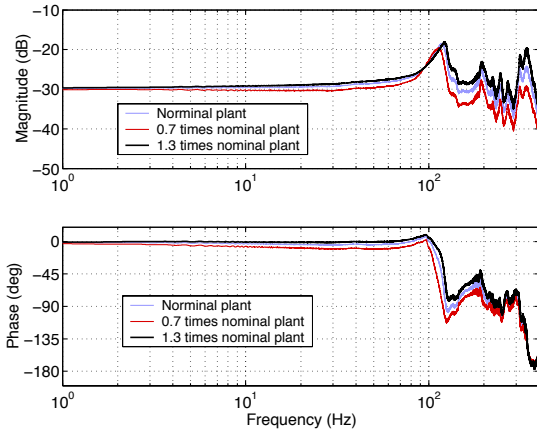


(a)

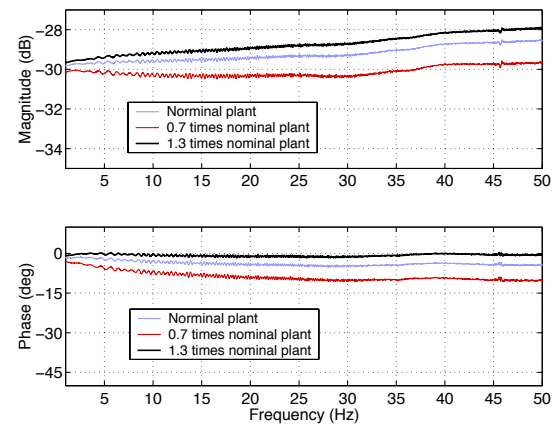


(b)

**Figure 3: Closed-loop transfer function of the first plant obtained using the first controller.**



(a)



(b)

**Figure 4: Closed-loop transfer function of the second plant obtained using the first controller.**

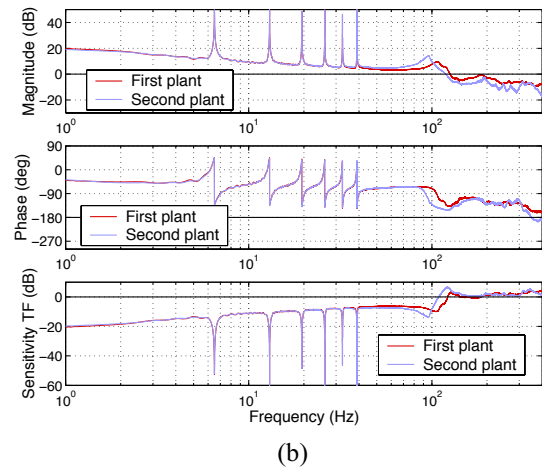
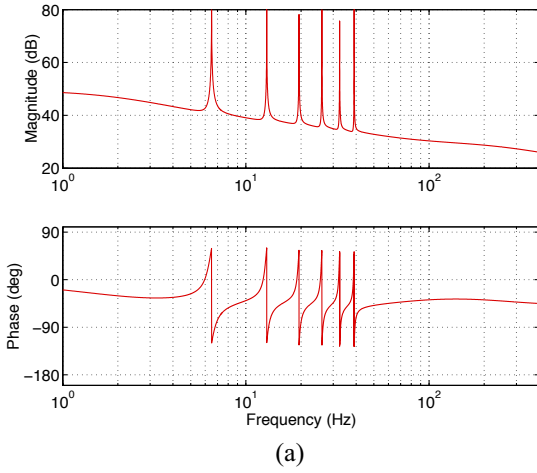


**Figure 5: Frequency response of the second controller (a) and its loop transfer function (b).**

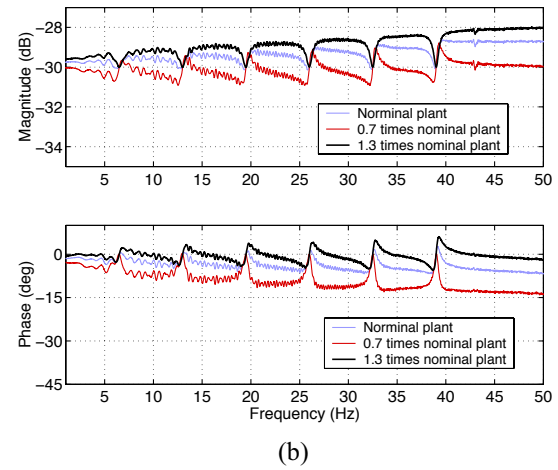
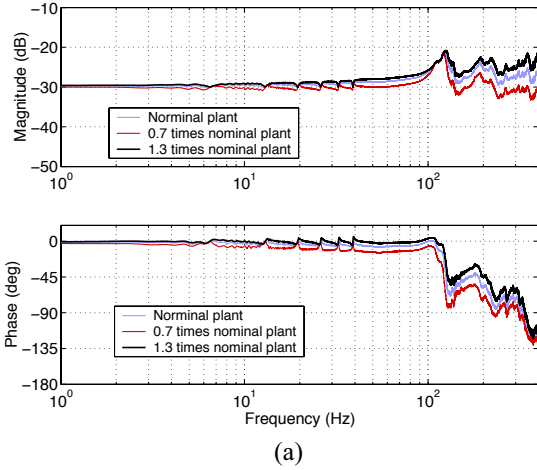


**Figure 6: Closed-loop transfer function of the first plant obtained using the second controller.**

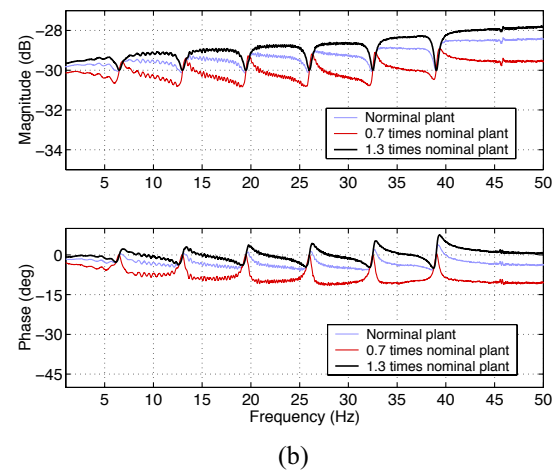
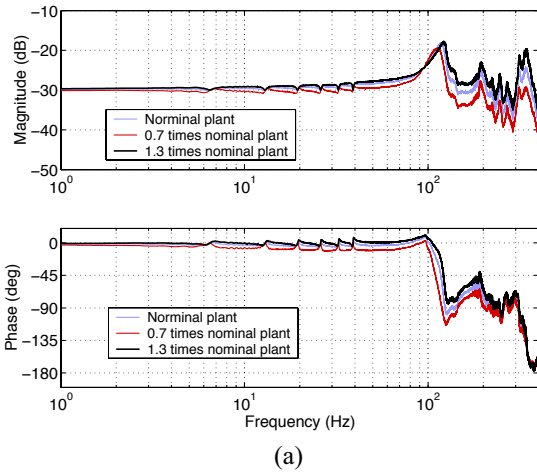


**Figure 7: Closed-loop transfer function of the second plant obtained using the second controller.**

### (3) The third controller: modern (model-based) & broadband controller

The first and second controllers were designed using the classical control design approach, where controllers are designed based on the measured transfer function without using any model. In the third controller design, we adopted a ‘modern approach’, in that a plant model is identified from the measured transfer function, and a controller is designed on the identified model. We also employed a ‘robust’ control design technique, considering that the actuator dynamics may change depending on its environment and that the controlled system should be able to function adequately regardless of the environmental uncertainty. Here, we assumed that there are two main uncertainties in the actuator system, which are the first resonant frequency and the DC gain (or, the scale factors). The controller was designed using the  $\mu$  synthesis technique (D-K iteration), so that the controlled actuator system can tolerate 15% of uncertainty in both the first resonant frequency and the DC gain, without degrading the closed-loop performance.

Note that we had to assume that the uncertainties in the resonant frequency and gain are complex, although they are actually real, because the current MATLAB version does not support *real  $\mu$  synthesis* (although it supports *real  $\mu$  analysis*). Since the controller obtained using the complex  $\mu$  synthesis may be conservative, we iterated the controller design via D-K iteration and used the real  $\mu$  analysis technique simultaneously, to check the robust stability and performance and improve the closed-loop performance.

Figure 8 shows the frequency response of measured and identified (i.e., model) transfer function of the actuator system. The frequency responses of the controller, the resulting loop transfer functions, and the sensitivity transfer functions are shown in Figure 9 – Figure 11. The loop transfer function in Figure 9(b) show that the third controller actually achieves at least 20dB of loop gain below 40 Hz, which is about 5 times higher than the first controller, with acceptable gain and phase margins. This indicates that the sensitivity of the closed-loop actuator system to uncertainty can be reduced at least by a factor of 10 below 40 Hz. The closed-loop transfer functions for each actuator response, which are shown in Figure 10 and Figure 11, respectively, support this expectation. The results in Figure 10 and Figure 11 show that the variation in the magnitude of the closed-loop actuator system with uncertainty is almost negligible below 40 Hz. This is a significant improvement of the closed-loop performance, compared with the first controller.

However, it should be reminded that the data we used to identify the actuator transfer function and design the controller has frequency components up to 400 Hz; we do not have any information about the dynamic behavior of the actuator above that frequency. Depending on the high-frequency dynamics of the actuator (which we do not know currently), the results shown here may be changed significantly.

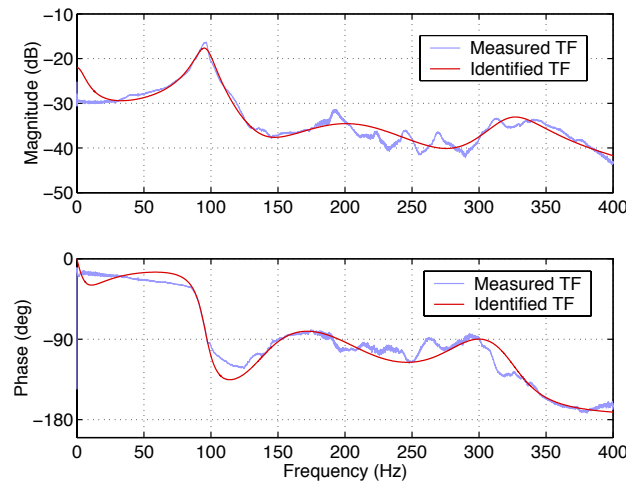
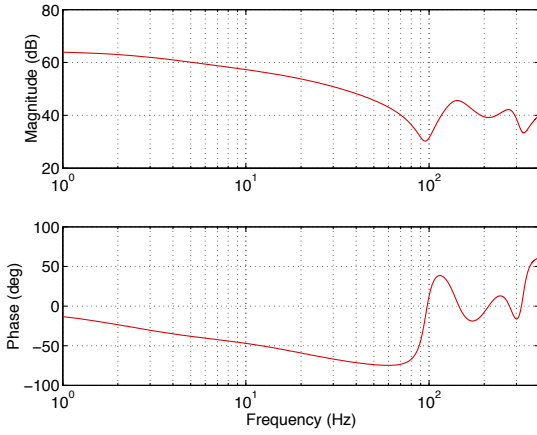
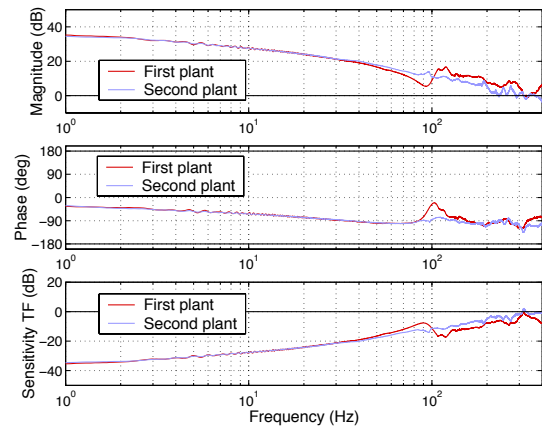


Figure 8: Measured and identified transfer function of the actuator.

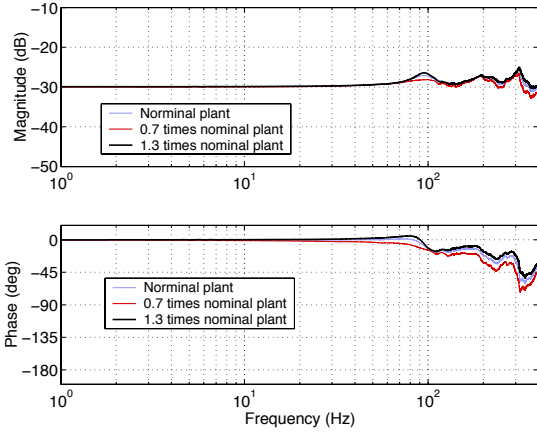


(a)

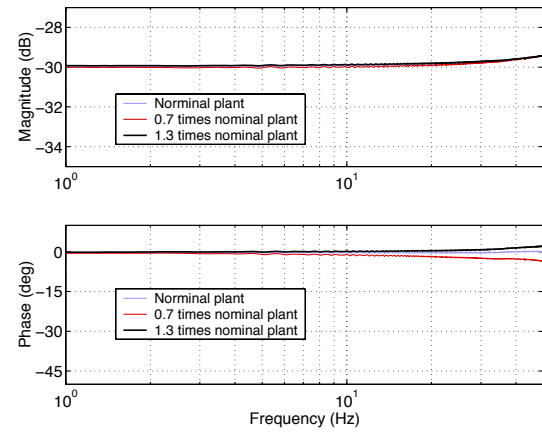


(b)

**Figure 9: Frequency response of the third controller (a) and its loop transfer function (b).**

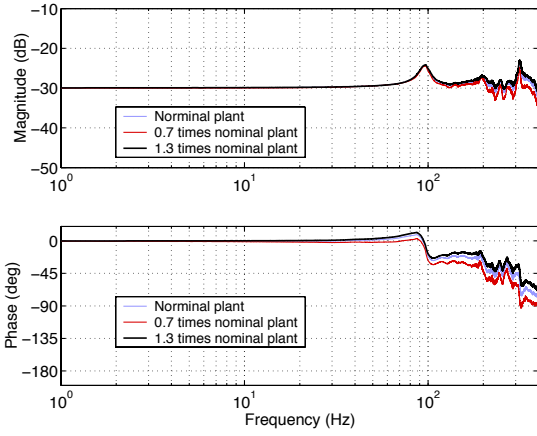


(a)

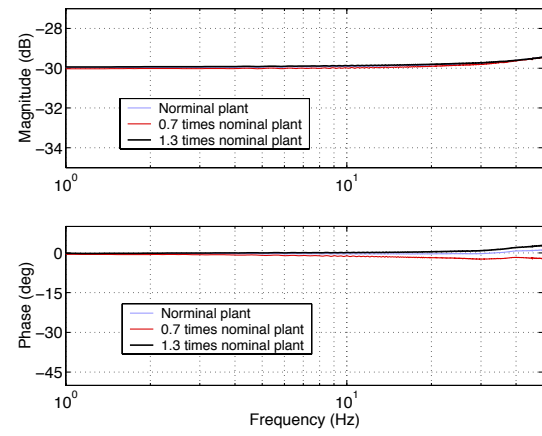


(b)

**Figure 10: Closed-loop transfer function of the first plant obtained using the third controller.**



(a)



(b)

**Figure 11: Closed-loop transfer function of the second plant obtained using the third controller.**

#### A.4 Discussions

As requested by Boeing, we have worked on the feasibility study of making X-frame actuator systems more robust using “inner loop” position controllers, to ensure that all flaps respond the same way. We investigated various feedback controllers on the open-loop frequency responses of X-frame actuator installed in the bench test rig, which were measured at Boeing in September 2002, in order to improve the robustness of the actuator system. The main conclusion of our work is that we can achieve roughly 50% of reduction in the sensitivity of the actuator to uncertainty below 40 Hz using the classical control approach, and at least 90 % of reduction using the modern control approach, without causing serious performance degradation above 100 Hz. If we want more reduction in the actuator’s sensitivity in the low frequency range, we have to accept worse performance in the high frequency range, and vice versa. Also, we can achieve quite high robustness of the actuator system at the harmonic frequencies using several higher harmonic controllers, as well as broadband feedback controllers.

Although the results of the feasibility study for the flap position control look promising, especially in the third controller (robust& model-based), the actual performance of X-frame actuator systems with the controller may not be as good as the simulation results, or even counter-productive, due to the following reasons:

- (1) As mentioned briefly before, we do not have any information about the dynamic behavior of the actuator above 400 Hz. The data we used to investigate the feasibility of the flap position control, which were taken at Boeing in September 2002, have frequency components up to 400 Hz. Therefore, the actual performance may be seriously worse depending on the high-frequency dynamics of the actuator, especially if the actuator system has some undesirable dynamics around 400Hz, such as high resonance and phase delay.
- (2) In order to achieve 20 dB of loop gain at 40 Hz, which will reduce the sensitivity of the actuator system to uncertainty by 90%, the bandwidth of the actuator should be at least 400 Hz, which seems significantly higher than the bandwidth of the current X-frame actuator.

Considering these facts, our recommendation is that the flap position control may be counter-productive, and therefore should not be used unless it is clear that the actuator deflections are significantly different from blade to blade.

## B System Identification of Linear Time Periodic Systems

We have improved our system identification methodologies to estimate the transfer functions of a linear time periodic (LTP) system. In spite of their importance, LTP systems have had much less attention than Linear Time Invariant (LTI) systems, primarily due to the complexity in analyzing LTP systems. Understanding the dynamic behavior of LTP systems is important in many engineering applications, especially the rotor system, in order to design effective control algorithms and improve the performance for those systems.

One of the fundamental differences between LTP and LTI systems remains in the frequency responses of those systems to a sinusoidal input. For LTI systems, a sinusoidal input at a given frequency produces the system output with the same frequency, with possibly different magnitude and phase. On the other hand, if a sinusoidal signal is input to LTP systems, possibly several (or an infinite number of) harmonics will appear in the output signal, each with possibly different magnitude and phase [1]. Due to these reasons, many analysis and controller design tools that have been developed for LTI systems, such as the concept of transfer functions, Bode and Nyquist theory, etc., cannot be directly applied to LTP systems.

This section describes our system identification methodologies for LTP systems, which were developed based on the work of Wereley [2]. The section is organized as follows. In Section B.1, an



overview of harmonic transfer functions and important properties of LTP systems are presented, along with a brief discussion on the development of the harmonic state-space model. Section B.2 deals with the theoretical development of two identification schemes we developed for determining harmonic transfer functions of LTP systems. The assumptions, simplifications, and noise reduction techniques of the schemes are also discussed. Section B.3 presents the validation results of our identification schemes by analyzing an LTP system, and comparing the transfer functions obtained analytically and empirically through our algorithms.

### B.1 Frequency Response of LTP Systems

In this section, we review briefly the characteristics of linear time periodic (LTP) systems and a linear operator to describe transfer properties of LTP systems. In LTP systems, the coefficients of the differential equations that describe the dynamics are time-varying and periodic. These systems are described by a state space model of the form

$$\dot{\mathbf{x}}(t) = \mathbf{A}(t)\mathbf{x}(t) + \mathbf{B}(t)\mathbf{u}(t), \mathbf{y}(t) = \mathbf{C}(t)\mathbf{x}(t) + \mathbf{D}(t)\mathbf{u}(t) \quad (1)$$

where the matrices  $\mathbf{A}(t)$ ,  $\mathbf{B}(t)$ ,  $\mathbf{C}(t)$ , and  $\mathbf{D}(t)$  are periodic with period  $T$ . In other words,

$$\mathbf{A}(t + NT) = \mathbf{A}(t), \mathbf{B}(t + NT) = \mathbf{B}(t), \mathbf{C}(t + NT) = \mathbf{C}(t), \mathbf{D}(t + NT) = \mathbf{D}(t) \quad (2)$$

for any integer  $N$ .

There is a fundamental difference in the frequency response between linear time invariant (LTI) systems and LTP systems. For LTI systems, the response to an input sinusoid at a single frequency is another sinusoid at the same frequency as the input signal, with possible changes in magnitude and phase. On the other hand, when a complex exponential (or sinusoid)  $e^{j\omega t}$  is used to excite an LTP system, the output response consists of a superposition of sinusoids not only at the input frequency  $\omega$ , but also at several (possibly an infinite number) other frequencies,  $\omega + n\omega_p$ , each with its own magnitude and phase [1], where  $n$  is an integer, and  $\omega_p = 2\pi/T$  is the pumping frequency. Since the frequencies  $n\omega_p$  are harmonics of the pumping frequency, the frequencies  $\omega + n\omega_p$  are shifted harmonics, and we often refer to these frequencies simply as “harmonics.”

As expected from the difference in the frequency response, a complex exponential  $e^{st}$ , which is an eigenfunction of LTI systems, cannot be an eigenfunction of LTP systems, because it results in a one to many map. In order to find eigenfunctions of LTP systems, Wereley et al. defined a complex exponentially modulated periodic (EMP) function, which is expressed as the complex Fourier series of a periodic signal of frequency  $\omega_p$ , modulated by a complex exponential signal [1],

$$u(t) = \sum_{n \in \mathbb{Z}} u_n e^{s_n t} \quad (3)$$

where  $s_n = s + jn\omega_p$  ( $s \in \mathbb{C}$ ). They showed that EMP functions are eigenfunctions of LTP systems, which implies that an LTP system induces at steady state a one-to-one map from EMP inputs to EMP outputs of the same frequency, but with possibly different magnitude and phase [1].

We should apply an EMP function to LTP systems to figure out their transfer properties, as we do for LTI systems using a complex exponential function. Since the steady state response of an LTP system in Equation 1 to an EMP function is also an EMP function, we can represent the state and output variables as

$$\mathbf{x}(t) = \sum_{n \in \mathbb{Z}} \mathbf{x}_n e^{s_n t}, \mathbf{y}(t) = \sum_{n \in \mathbb{Z}} \mathbf{y}_n e^{s_n t} \quad (4)$$

Also, the time periodic coefficient matrix in Equation 1 can be expanded in a complex Fourier series as

$$\mathbf{A}(t) = \sum_{m \in \mathbb{Z}} \mathbf{A}_m e^{jm\omega_p t}, \mathbf{B}(t) = \sum_{m \in \mathbb{Z}} \mathbf{B}_m e^{jm\omega_p t}, \mathbf{C}(t) = \sum_{m \in \mathbb{Z}} \mathbf{C}_m e^{jm\omega_p t}, \mathbf{D}(t) = \sum_{m \in \mathbb{Z}} \mathbf{D}_m e^{jm\omega_p t} \quad (5)$$

Using Equation 4 and 5, and applying the harmonic balance approach, the state space model in Equation 1 can be transformed in the frequency domain as

$$s_n \mathbf{x}_n = \sum_{m \in \mathbb{Z}} \mathbf{A}_{n-m} \mathbf{x}_m + \sum_{m \in \mathbb{Z}} \mathbf{B}_{n-m} \mathbf{u}_m, \mathbf{y}_n = \sum_{m \in \mathbb{Z}} \mathbf{C}_{n-m} \mathbf{x}_m + \sum_{m \in \mathbb{Z}} \mathbf{D}_{n-m} \mathbf{u}_m \quad (6)$$

After expressing the summations in matrix form, the equations reduce to

$$sX = (A - N)X + BU, Y = CX + DU \quad (7)$$

The state vector  $X$  represents the states at various harmonics of a given frequency, and is defined as

$$X^T = [\cdots \mathbf{x}_{-2}^T \mathbf{x}_{-1}^T \mathbf{x}_0^T \mathbf{x}_1^T \mathbf{x}_2^T \cdots] \quad (8)$$

The control signal,  $U$ , and output signal,  $Y$ , are similarly defined. The dynamics matrix  $A$  is a doubly-infinite Toeplitz matrix, given by

$$A = \begin{bmatrix} \ddots & \vdots & \vdots & \vdots & \\ \cdots & \mathbf{A}_0 & \mathbf{A}_{-1} & \mathbf{A}_{-2} & \cdots \\ \cdots & \mathbf{A}_1 & \mathbf{A}_0 & \mathbf{A}_{-1} & \cdots \\ \cdots & \mathbf{A} & \mathbf{A}_1 & \mathbf{A}_0 & \cdots \\ & \vdots & \vdots & \vdots & \end{bmatrix} \quad (9)$$

The matrix  $\mathbf{A}_n$  is the  $n$ th Fourier coefficient of  $\mathbf{A}(t)$ . The matrices  $B$ ,  $C$ , and  $D$  are similarly defined. The modulation frequency matrix,  $N$ , is an infinite block diagonal matrix, given by

$$N = \begin{bmatrix} & & & & & \\ & -2 \cdot j\omega_p \mathbf{I} & & & & 0 \\ & & -1 \cdot j\omega_p \mathbf{I} & & & \\ & & & 0 \cdot j\omega_p \mathbf{I} & & \\ & & & & 1 \cdot j\omega_p \mathbf{I} & \\ 0 & & & & & 2 \cdot j\omega_p \mathbf{I} \end{bmatrix} \quad (10)$$

where  $\mathbf{I}$  is the identity matrix of the same dimensions as that of  $\mathbf{A}_n$ .

The harmonic transfer function (HTF) is defined as an operator that relates harmonics of the input signal to harmonics of the output signals, and is given by [1]

$$G(s) = C[s\mathbf{I} - (A - N)]^{-1} B + D \quad (11)$$

The LTP transfer function is thus analogous to the widely used LTI transfer function, in that it describes the input-output properties of LTP systems in the frequency domain. It should be noted that the expression for harmonic transfer functions of LTP systems in Equation 11 has a very similar form as that for transfer functions of LTI systems. Although the matrices in Equation 7 are infinite (due to the infinite Fourier coefficients), for practical purposes we can truncate the number of terms in the Fourier series, and simply use the smallest number of harmonics that adequately represent the system dynamics. Since the harmonics generally get smaller with increasing harmonic number, only the consideration of the first few harmonics is usually adequate in describing the system behavior.

We can now employ this notion of harmonic transfer functions in developing methods for system identification of LTP systems.

## B.2 System Identification Schemes for LTP systems

In this section, we present our approaches to identify harmonic transfer functions of LTP systems. We first illustrate the difficulties encountered when identifying LTP systems, and the two different approaches we developed to overcome these difficulties will be described in detail.

### Challenges in LTP System Identification

In an LTP system, an input sinusoid at a single frequency generates a superposition of sinusoids at infinite frequencies of various magnitudes and phase in the output. This frequency behavior of LTP systems is fundamentally different from that of LTI systems, where an input sinusoid at a single frequency generates an output sinusoid at the same frequency as the input signal. Due to the different behaviors in the frequency domain between LTP and LTI systems, the method of estimating LTI transfer functions, which is well established, cannot be used to estimate harmonic transfer functions (HTF) of an LTP system.

To illustrate the difficulty of identifying LTP systems, we will initially account for only three frequencies in the output of an LTP system, for each input frequency. The LTP system will have period  $T$ , and corresponding fundamental frequency  $\omega_p$ . We therefore assume that the output,  $Y$ , at each frequency  $\omega$ , comprises of the linear combination of the responses due to inputs at frequencies  $\omega$ ,  $\omega + \omega_p$  and  $\omega - \omega_p$ . The system output can then be assumed to be a linear combination of three different transfer functions (each corresponding to one of the three frequencies in the output):  $G_0$ ,  $G_1$ , and  $G_{-1}$ , respectively.  $Y$  can thus be expressed as

$$Y(j\omega) = G_0(j\omega)U(j\omega) + G_1(j\omega)U(j\omega - j\omega_p) + G_{-1}(j\omega)U(j\omega + j\omega_p) \quad (12)$$

Equivalently in the time domain, the output may be written as

$$y(t) = g_0(t) * u(t) + g_1(t) * [u(t)e^{j\omega_p t}] + g_{-1}(t) * [u(t)e^{-j\omega_p t}] \quad (13)$$

where  $g_k(t)$  is the  $k$ th impulse response of the system, and '\*' denotes the convolution operator.

From Equation 13, one can see that the output  $y(t)$  is defined as the total response due to an input  $u(t)$  that has been modulated appropriately, and then convolved with the respective impulse response functions. We can state more specifically that the  $n$ th transfer function is defined to be the linear operator that maps the output at frequency  $\omega$  to an input, at frequency  $\omega$ , modulated with  $e^{j\omega_p t}$ . This linear system can be represented in the block diagram of Figure 12.

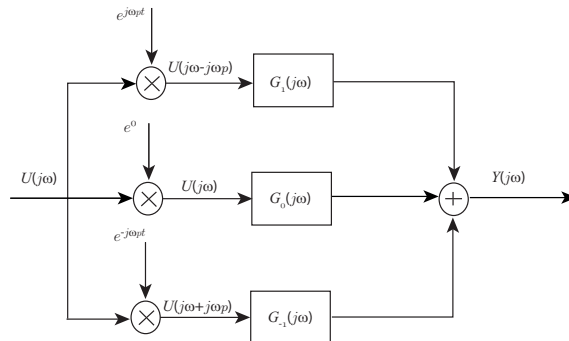


**Figure 12: LTP system model with three transfer functions.**

As is evident from Equations 12 and 13, we have three transfer functions,  $G_0$ ,  $G_1$ , and  $G_{-1}$ , that need to be estimated. For a given input  $U(j\omega)$  and resulting output  $Y(j\omega)$ , we thus have three unknowns, but only one equation. Our identification problem is therefore underdetermined. In order to overcome this

difficulty, we have developed two different approaches that allow us to estimate HTFs of an LTP system systematically. The following subsections describe our system identification methods for LTP systems.

### First method

The basic idea of the first method is to assume that the transfer functions are “smooth” and to formulate the original problem as the minimization of a cost function that penalizes the quadratic estimation error and the curvature of harmonic transfer functions (HTFs) [3]. Here, “smooth” transfer functions mean that there are no rapid variations with frequency in the response. By using this approach, the originally underdetermined problem becomes determinate, and therefore, the HTFs of LTP systems can be estimated without any difficulty. In order to estimate the transfer functions with enough accuracy, the input signal used to excite the system should have enough frequency components, and the time length of the input signal should be much greater than the period of the system.

The procedure of estimating HTFs of LTP systems using the first method is described in detail. We need three sets of data to estimate the transfer functions for LTP systems, specifically the input  $u$ , output  $y$ , and time measurements (at which  $u$  and  $y$  occur)  $\psi$ . The data is assumed to have been digitally acquired, hence all the data points can be assembled in a vector of length  $n$ , where  $n$  is the total number of data points. Each data point is essentially a digital record of the measurement of an analog signal determined at some fixed sampling frequency. The input data is therefore expressed as

$$u = [u_1 \quad u_2 \quad u_3 \quad \cdots \quad u_n] \quad (14)$$

$y$  and  $\psi$  are similarly defined.

The total number of transfer functions of the system that need to be identified,  $n_h$ , have to be specified in advance. An  $n_h \times n$  matrix  $\mathbf{U}$  is defined, where each row consists of an appropriately modulated and Fourier transformed data vector  $\mathbf{u}$ , given as

$$\mathbf{U} = \begin{bmatrix} F\left\{ \begin{bmatrix} e^{jm\psi_1 u_1} & \cdots & \cdots & e^{jm\psi_1 u_n} \end{bmatrix} \right\} \\ \vdots & & \vdots & \vdots \\ F\left\{ \begin{bmatrix} e^{j0\psi_1 u_1} & \cdots & \cdots & e^{j0\psi_1 u_n} \end{bmatrix} \right\} \\ \vdots & & \vdots & \vdots \\ F\left\{ \begin{bmatrix} e^{-jm\psi_1 u_1} & \cdots & \cdots & e^{-jm\psi_1 u_n} \end{bmatrix} \right\} \end{bmatrix} \quad (15)$$

where  $m = (n_h - 1)/2$ . In more compact notation, the  $\mathbf{U}$  matrix is really

$$\mathbf{U}^T = \left[ \mathbf{u}^T(\omega - m\omega_p) \quad \cdots \quad \mathbf{u}^T(\omega) \quad \cdots \quad \mathbf{u}^T(\omega + m\omega_p) \right] \quad (16)$$

where  $\mathbf{u}(\omega)$  is the discrete Fourier transform of  $u$ . Similarly, we define a  $\mathbf{Y}$  matrix as the discrete Fourier transform of vector  $y$

$$\mathbf{Y} = F\left\{ \begin{bmatrix} y_1 & y_2 & y_3 & \cdots & y_n \end{bmatrix} \right\} \quad (17)$$

When identifying LTI systems, we usually compute the cross- and power spectral densities of input and output signals, and estimate the transfer function of the system. We employ similar concepts for LTP systems, in that we define the power spectral density of input signal  $\Phi_{UU}$ , and the cross spectral density of input and output signal  $\Phi_{UY}$  as

$$\Phi_{UU} = \mathbf{U}^{*T} \mathbf{U}, \quad \Phi_{UY} = \mathbf{U}^{*T} \mathbf{Y} \quad (18)$$

where  $\mathbf{U}^{*T}$  is complex conjugate transpose of  $\mathbf{U}$ . If we want to reduce the effect of noise, we may use  $N$  different input and output signal, and average the power- and cross-spectrum as

$$\Phi_{UU} = \frac{1}{N} \sum_{k=1}^N \mathbf{U}_k^{*T} \mathbf{U}_k, \Phi_{UY} = \frac{1}{N} \sum_{k=1}^N \mathbf{U}_k^{*T} \mathbf{Y}_k \quad (19)$$

It is important to note that ordinary matrix multiplication is not performed in the computation of  $\Phi_{UU}$  and  $\Phi_{UY}$  in Equation 18. Rather, each column vector of  $\mathbf{U}$  is transposed to form a row vector, and multiplied with its corresponding column vector to yield an  $n_h \times n_h$  matrix. Each of these matrices is assembled in a three dimensional  $n_h \times n_h \times n$  array to form  $\Phi_{UU}$ .  $\Phi_{UY}$  is similarly constructed as an  $n_h \times 1 \times n$  array. For example, the  $n_h \times n_h$  matrix in the  $i$ th position of the third dimension of  $\Phi_{UU}$  is given as (denoted as  $\Phi_{UU_i}$ )

$$\Phi_{UU_i} = \begin{bmatrix} u_i(\omega - m\omega_p) \\ \vdots \\ u_i(\omega) \\ \vdots \\ u_i(\omega + m\omega_p) \end{bmatrix}^* \begin{bmatrix} u_i(\omega - m\omega_p) & \cdots & u_i(\omega) & \cdots & u_i(\omega + m\omega_p) \end{bmatrix} \quad (20)$$

Similarly for the  $\Phi_{UY}$  array, the  $i$ th vector in its third dimension is

$$\Phi_{UY_i}^T = \begin{bmatrix} u_i^*(\omega - m\omega_p) y_i(\omega) & \cdots & u_i^*(\omega) y_i(\omega) & \cdots & u_i^*(\omega + m\omega_p) y_i(\omega) \end{bmatrix} \quad (21)$$

We can now write an expression that represents HTFs of LTP systems as

$$\Phi_{UY} = \Phi_{UU} \bullet \hat{\mathbf{G}} \quad (22)$$

Here,  $\hat{\mathbf{G}}$  is an  $n_h \times 1 \times n$  array representing HTFs of LTP systems. The  $i$ th vector of  $\hat{\mathbf{G}}$  in its third dimension is given as

$$\mathbf{g}_i^T = \begin{bmatrix} g_{m_i} & \cdots & g_{1_i} & g_{0_i} & g_{-1_i} & \cdots & g_{-m_i} \end{bmatrix} \quad (23)$$

Again, the ordinary matrix multiplication is not performed in Equation 22. The meaning of the computation in Equation 22 is that we can apply the ordinary matrix multiplication to the  $i$ th matrix (or, vector) of  $\Phi_{UY}$ ,  $\Phi_{UU}$ , and  $\hat{\mathbf{G}}$ . That is,

$$\Phi_{UY_i} = \Phi_{UU_i} \mathbf{g}_i \quad (24)$$

It should be noted that Equation 24 may be underdetermined or determinate, depending on whether  $n_h=1$  or not. Consider first the case  $n_h=1$ . In this case, only the fundamental transfer function ( $g_0$ ) needs to be identified, and  $\Phi_{UU}$  and  $\Phi_{UY}$  reduce to  $1 \times 1 \times n$  arrays, where  $\Phi_{UU_i}$  is  $|u_i(\omega)|^2$ , and  $\Phi_{UY_i}$  is  $u_i^*(\omega) y_i(\omega)$ . Each element of  $g_0$  is given as

$$g_{0_i}(\omega) = \frac{u_i^*(\omega) y_i(\omega)}{|u_i(\omega)|^2} \quad (25)$$

which is the same relation as that used to estimate the transfer function for LTI systems. Thus, this scheme reduces to LTI system identification if only one transfer function is considered in the calculations.

For  $n_h > 1$ , however,  $\Phi_{UU_i}$  matrix is not positive definite, and therefore not invertible. That is, the problem becomes underdetermined, which implies that we cannot compute  $\mathbf{g}_i$  just by inverting  $\Phi_{UU_i}$  and multiplying it to  $\Phi_{UY_i}$  in Equation 24. As mentioned earlier, the reason for the non-invertibility of  $\Phi_{UU_i}$  is that we have  $n_h$  unknowns, but only one equation.

The solution we adopt to overcome this difficulty is to assume that the transfer functions are smooth, and to formulate the original problem as the minimization of a cost function that penalizes the quadratic estimation error and the curvature of HTFs. To describe our algorithm in more detail and clearly, the issues of the estimation error and the curvature of the transfer functions are presented. The estimation error occurs because we have made a simplification in our analysis, and have considered only a few harmonics, although there are in general infinite harmonics in LTP systems. For instance, suppose a given system has  $N_h$  transfer functions of relatively significant magnitudes, but only  $n_h$  of them are evaluated through this method. In that case, the system has been modeled with  $n_h$  number of transfer functions, and its output response due to an input may be expressed as

$$\mathbf{Y} = \underbrace{\sum_{k=-m}^m \mathbf{u}(\omega - k\omega_p) \mathbf{g}_k}_{\text{modeled part}} + \underbrace{\sum_{m < |l| \leq M} \mathbf{u}(\omega - l\omega_p) \mathbf{g}_l}_{\text{unmodeled part}} \quad (26)$$

where  $m = (n_h - 1)/2$  and  $M = (N_h - 1)/2$ . The unmodeled part essentially appears as an error,  $\mathbf{e}$ , in our output equation for the identification scheme, since only the modeled part is considered in the identification procedure. Therefore,

$$\mathbf{Y} = \sum_{k=-m}^m \mathbf{u}(\omega - k\omega_p) \mathbf{g}_k + \mathbf{e} = \mathbf{U}^T \hat{\mathbf{G}} + \mathbf{e} \quad (27)$$

In addition to reducing the estimation error  $\mathbf{e}$ , we also need to make assumptions so that the identification problem is well-posed. In this regard, we assume that the transfer functions are smooth, i.e., there are no rapid variations (with frequency) in the transfer functions. This is a reasonable assumption, since rapid variations with frequency in a transfer function usually are not physical.

In order to reduce  $\mathbf{e}$ , and to apply the assumption we have just made, we formulate our problem as the minimization of a cost function,  $J$ , that penalizes the quadratic error and the curvature of the transfer functions, so that [3]

$$J = \min \left[ \left( \mathbf{Y} - \mathbf{U}^T \hat{\mathbf{G}} \right)^2 + \alpha \left( \mathbf{D} \hat{\mathbf{G}} \right)^2 \right] \quad (28)$$

where  $\mathbf{D}^2$  is the second difference operator approximating the second derivative, given as

$$\mathbf{D}^2 = \begin{bmatrix} -2 & 1 & & & \\ 1 & & \ddots & & \\ & \ddots & & & 1 \\ & & & 1 & -2 \end{bmatrix} \quad (29)$$

and  $\alpha$  is a constant. It is evident from Equation 28 that by selecting various values for  $\alpha$ , we can weight the second derivatives of  $\hat{\mathbf{G}}$  more or less in the cost function, and thus penalize the curvature so that rapid variations with frequency in  $\hat{\mathbf{G}}$  are reduced. In order to get a closed form expression for  $\hat{\mathbf{G}}$ , Equation 28 is evaluated by taking the derivative of  $J$  with respect to  $\hat{\mathbf{G}}$ , setting it equal to zero, and then solving for  $\hat{\mathbf{G}}$ , which gives

$$\hat{\mathbf{G}} = [\mathbf{U}^T \mathbf{U} + \alpha \mathbf{D}^4]^{-1} \mathbf{U}^T \mathbf{Y} \quad (30)$$

where  $\mathbf{D}^4 = \mathbf{D}^2 \cdot \mathbf{D}^2$ . Recall that we had assembled  $\mathbf{U}^T \mathbf{U}$  and  $\mathbf{U}^T \mathbf{Y}$  in three dimensional arrays,  $\Phi_{\mathbf{U}\mathbf{U}}$  and  $\Phi_{\mathbf{U}\mathbf{Y}}$ , respectively. However, in order to numerically evaluate Equation 30, we need to reduce these arrays into two-dimensional matrices. The  $\Phi_{\mathbf{U}\mathbf{U}}$  array is therefore transformed into a square, block diagonal,  $n_\Phi \times n_\Phi$  matrix  $\Phi_{\mathbf{U}\mathbf{U}s}$ , in which the  $i$ th block is  $\Phi_{\mathbf{U}\mathbf{U}i}$ , and  $n_\Phi = n_h \times n$ . Thus,  $\Phi_{\mathbf{U}\mathbf{U}s}$  has the form as illustrated in Figure

13(a). Similarly,  $\Phi_{UY}$  is transformed into a column vector  $\Phi_{uy}$ , of length  $n_\phi$ , with the form as shown in Figure 13(b).

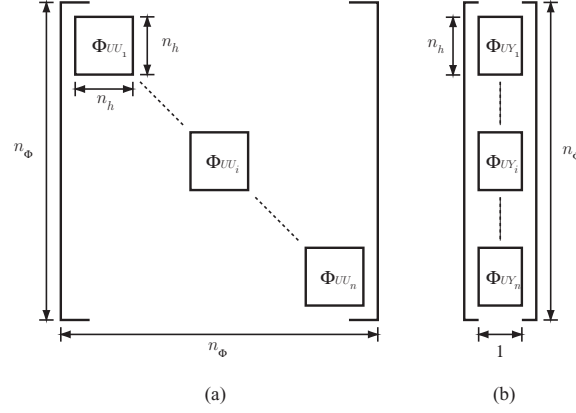


**Figure 13: (a) Structure of  $\Phi_{UU_s}$ . (b) Structure of  $\Phi_{uy}$ .**

The  $\hat{\mathbf{G}}$  matrix is also transformed into a vector  $\hat{\mathbf{g}}$ , where  $\hat{\mathbf{g}}$  has  $n$  sub-vectors of length  $n_h$ , each of which is a column vector of  $\hat{\mathbf{G}}$ . Equation 30 then becomes

$$\hat{\mathbf{g}} = [\Phi_{UU_s} + \alpha \tilde{\mathbf{D}}^4]^{-1} \Phi_{uy} \quad (31)$$

where  $\tilde{\mathbf{D}}^4$  indicates the change of the dimensions of  $\mathbf{D}^4$ , similar to the change in dimensions going from  $\mathbf{U}^T \mathbf{U}$  to  $\Phi_{UU_s}$ . Now, the original underdetermined problem in Equation 24 is transformed into the determinate one in Equation 31 by adopting the assumption about the smoothness of the transfer functions. Using Equation 31, we can estimate the HTFs of LTP systems, given the input signal and measured output response. Here, the weighting factor  $\alpha$  should be selected carefully such that the transfer functions become smoothed out enough, while capturing the important features of the systems. Note that too much smoothing, i.e., too high value of  $\alpha$ , may overestimate the system damping, and therefore, the results of the system identification may be inaccurate.

The advantage of the first method is that we can generate an input signal quite easily to estimate the HTFs. That is, the results of system identification using this method are quite insensitive to the input signal, as long as the input signal has enough frequency components and time length. As will be shown in the next section, this is a significant advantage over the second method, whose solutions are sensitive to small errors in the input signal.

However, the first approach needs some ad-hoc manners to transform the originally underdetermined problem into the determinate one, and therefore to estimate the HTFs. In addition, this approach requires much computer memory and intensive computational procedure, because we should take into account the power spectral density  $\Phi_{UU_s}$  and cross-spectral density matrix  $\Phi_{uy}$  of input and output spectrum with all frequencies simultaneously.

### **Second method**

The second approach we developed to solve the underdetermined problem is to apply  $n_h$  inputs and measure the resulting outputs, in order to estimate  $n_h$  harmonic transfer functions. We can thus form  $n_h$  independent equations of the form of Equation 12, and will subsequently be able to evaluate the desired transfer functions. This approach allows us to avoid the use of the heuristic assumption that the transfer functions are smooth, and therefore, we can address the problem more naturally. In order to use this approach successfully, however, we should be extremely careful in designing input signals to excite LTP systems, compared with the first approach. That is, it is very important to take into consideration the time of application of each input relative to the system period. This is due to the time-varying nature of the

system dynamics during one period. If the system behavior is to be completely characterized, the system needs to be excited with appropriate input signals at various times in its period  $T$ . When  $n_h$  transfer functions are being evaluated, at least the same number of identical input signals should be applied that are evenly spread out over the system period. Figure 14 depicts when each of the  $n_h$  inputs should be initiated, relative to the system period.

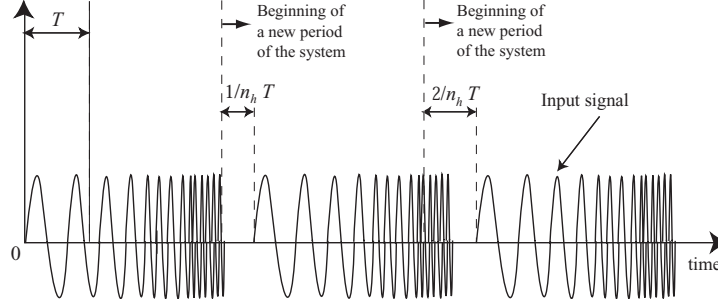


**Figure 14: Input signals initiated at appropriate time intervals over the system periods.**

We define  $T_d$ , as the amount of time (in seconds) elapsed between the beginning of a new period of the system and the start of the first input signal since the beginning of that particular period. In this specific case, where we have just established that the  $n_h$  inputs should be spaced uniformly apart,  $T_d$  is given as

$$T_d = \frac{T}{n_h} = \frac{2\pi}{n_h \omega_p} \quad (32)$$

The first input should have zero delay between the start of a system period and its time of initiation. The response of the LTP system output,  $y_0(t)$ , due to the first input,  $u(t)$ , is given by

$$y_0(t) = \sum_{k=-m}^m g_k(t) * [u(t)e^{jk\omega_p t}] \quad (33)$$

where  $m = (n_h - 1)/2$ , '\*' denotes the convolution operator, and  $g_k(t)$  is the  $k$ th harmonic impulse response of the system. The input  $U = F\{u(t)\}$ , and output  $Y_0 = F\{y_0(t)\}$ , to the system for  $n_h = 3$  in the frequency domain are modeled as depicted in Figure 12.

For the second chirp, there should be a delay of  $T_d$  seconds between the start of a system period and its time of application, so the actual input will be  $u(t - T_d)$ . The system output due to this second chirp,  $y_1(t)$ , is given by

$$y_1(t - T_d) = \sum_{k=-m}^m g_k(t) * [u(t - T_d)e^{jk\omega_p t}] \quad (34)$$

Repeating the procedure described above, the system output due to the  $n$ th chirp,  $y_n(t)$ , will be expressed as in the time domain

$$y_n(t - nT_d) = \sum_{k=-m}^m g_k(t) * [u(t - nT_d)e^{jk\omega_p t}], 0 \leq n \leq n_h \quad (35)$$

Therefore, the relation between the  $n$ th chirp input and its resulting system output in the frequency domain is given as

$$Y_n(j\omega)e^{-jnT_d\omega} = \sum_{k=-m}^m G_k(j\omega)U(j\omega - jk\omega_p)e^{-jnT_d\omega}e^{jk\omega_p T_d}, 0 \leq n \leq n_h \quad (36)$$



## **Table of Contents (including Appendices)**

<b>TABLE OF CONTENTS (INCLUDING APPENDICES)</b> .....	<b>2</b>
<b>TABLE OF ILLUSTRATIONS AND TABLES</b> .....	<b>3</b>
<b>1. STATEMENT OF PROBLEM STUDIED</b> .....	<b>4</b>
<b>2. SUMMARY OF IMPORTANT RESULTS</b> .....	<b>4</b>
<b>3. PAPERS SUBMITTED OR PUBLISHED</b> .....	<b>7</b>
<b>4. SCIENTIFIC PERSONNEL</b> .....	<b>7</b>
<b>5. REPORT OF INVENTIONS</b> .....	<b>7</b>
<b>6. BIBLIOGRAPHY (CITED ABOVE AND IN APPENDICES)</b> .....	<b>8</b>
<b>A FLAP POSITION CONTROL LOOP</b> .....	<b>9</b>
A.1 BASIC CONCEPT OF FLAP POSITION CONTROL LOOP .....	9
A.2 TRANSFER FUNCTION OF ACTUATOR SYSTEMS .....	9
A.3 DESIGN OF CONTROLLERS AND SIMULATION RESULTS .....	10
A.4 DISCUSSIONS .....	16
<b>B SYSTEM IDENTIFICATION OF LINEAR TIME PERIODIC SYSTEMS</b> .....	<b>16</b>
B.1 FREQUENCY RESPONSE OF LTP SYSTEMS .....	17
B.2 SYSTEM IDENTIFICATION SCHEMES FOR LTP SYSTEMS .....	19
B.3 VALIDATION OF SYSTEM IDENTIFICATION METHODS .....	27
<b>C SUMMARY OF WIND TUNNEL TEST AT LANGLEY</b> .....	<b>34</b>
C.1 SYSTEM IDENTIFICATION OF ROTOR SYSTEMS .....	35
C.2 CLOSED-LOOP EXPERIMENTAL RESULTS .....	39

where  $Y_n(j\omega)$ ,  $U(j\omega)$ , and  $G_k(j\omega)$  are Fourier transform of  $y_n(t)$ ,  $u(t)$ , and  $g_k(t)$ , respectively. It should be noted that the Fourier transform of  $u(t - nT_d)e^{jk\omega_p t}$  is  $U(j\omega - jk\omega_p)e^{-jnT_d\omega}e^{jk\omega_p T_d}$ . Combining all of the system response, the output vector  $\mathbf{Y}^T = [Y_0 Y_1 \dots Y_{n_h-1}]$  can be expressed as

$$\underbrace{\begin{bmatrix} Y_0 \\ \vdots \\ Y_n \\ \vdots \\ Y_{n_h-1} \end{bmatrix}}_{\mathbf{Y}} = \underbrace{\begin{bmatrix} U_m & \cdots & U_0 & \cdots & U_{-m} \\ \vdots & \ddots & \vdots & & \vdots \\ U_m W^{-mn} & & U_0 & & U_{-m} W^{mn} \\ \vdots & & \vdots & \ddots & \vdots \\ U_m W^{-m(n_h-1)} & \cdots & U_0 & \cdots & U_{-m} W^{m(n_h-1)} \end{bmatrix}}_{\mathbf{U}} \cdot \underbrace{\begin{bmatrix} G_{-m} \\ \vdots \\ G_k \\ \vdots \\ G_m \end{bmatrix}}_{\mathbf{G}} \quad (37)$$

where  $U_m = U(j\omega + jm\omega_p)$ , and  $W = e^{j\omega_p T_d}$ . Multiplying  $\mathbf{U}^{*T}$  to both sides of Equation 37 yields

$$\Phi_{\mathbf{U}\mathbf{Y}} = \Phi_{\mathbf{U}\mathbf{U}} \mathbf{G} \quad (38)$$

where  $\Phi_{\mathbf{U}\mathbf{Y}} = \mathbf{U}^{*T} \mathbf{Y}$  and  $\Phi_{\mathbf{U}\mathbf{U}} = \mathbf{U}^{*T} \mathbf{U}$ . As in the first method, we can use  $N$  different input and output signal and average the power- and cross-spectrum, in order to reduce the effect of noise. In that case,  $\Phi_{\mathbf{U}\mathbf{U}}$  and  $\Phi_{\mathbf{U}\mathbf{Y}}$  are given as

$$\Phi_{\mathbf{U}\mathbf{U}} = \frac{1}{N} \sum_{k=1}^N \mathbf{U}_k^{*T} \mathbf{U}_k, \quad \Phi_{\mathbf{U}\mathbf{Y}} = \frac{1}{N} \sum_{k=1}^N \mathbf{U}_k^{*T} \mathbf{Y}_k \quad (39)$$

In contrast to the first approach, the power spectral density of the input signal  $\Phi_{\mathbf{U}\mathbf{U}}$  is not singular in the second approach. The reason for the invertibility of  $\Phi_{\mathbf{U}\mathbf{U}}$  is that we consider at least the same number of the input signals as that of the HTFs to be identified. Therefore, we can compute the HTFs vector  $\mathbf{G}$  from Equation 38 just by inverting  $\Phi_{\mathbf{U}\mathbf{U}}$  and multiplying it to  $\Phi_{\mathbf{U}\mathbf{Y}}$ , as

$$\mathbf{G} = \Phi_{\mathbf{U}\mathbf{U}}^{-1} \Phi_{\mathbf{U}\mathbf{Y}} \quad (40)$$

Equation 40 can be further simplified, so that the  $k$ th HTF,  $G_k$ , can be obtained after some mathematical manipulations, as (for  $N=1$ )

$$G_k(j\omega) = \frac{U^*(j\omega - jk\omega_p) \sum_{n=0}^{n_h-1} Y_n(j\omega) W^{kn}}{n_h |U(j\omega - jk\omega_p)|^2} \quad (41)$$

It should be noted that the computation of  $\mathbf{G}$  in Equation 40 can be performed at each frequency independently. That is,  $\Phi_{\mathbf{U}\mathbf{U}}$  is an  $n_h \times n_h$  matrix, and therefore, the number of data points is not involved in the inverse matrix computation of  $\Phi_{\mathbf{U}\mathbf{U}}$ . This makes a critical difference between the first and the second method. Recalling from Equation 31 is an  $nn_h \times nn_h$  matrix ( $n$  is the number of data points), we have observed that the first approach requires us to consider the whole frequency response simultaneously to estimate HTFs.

Equation 40 will yield HTFs of LTP systems with reasonable accuracy, if the effect of noise is not significant. However, if the system output is so severely corrupted by noise that the averaging in Equation 39 is not enough to reduce the effect of noise, some smoothing schemes should be employed to generate transfer functions with acceptable accuracy. First, we can convolve the averaged power- and cross-spectrum in the frequency domain with smoothing window functions. The smoothed power- and cross-spectrum are given by

$$\hat{\Phi}_{\mathbf{U}\mathbf{U}} = \Phi_{\mathbf{U}\mathbf{U}} * w(\omega), \quad \hat{\Phi}_{\mathbf{U}\mathbf{Y}} = \Phi_{\mathbf{U}\mathbf{Y}} * w(\omega) \quad (42)$$

where  $w(\omega)$  is a window function and '\*' is a convolution operator, both defined in the frequency domain. Various window functions can be used here, such as a rectangular, Hanning, Balett window, etc., depending on the applications. The smoothed HTF is obtained by taking the ratio of the smoothed cross- and power spectrum as

$$\hat{\mathbf{G}} = \hat{\Phi}_{UU}^{-1} \hat{\Phi}_{UY} \quad (43)$$

The smoothing technique in Equation 43 reduces the effect of measurement noise quite effectively and leads to an accurate estimate of the transfer functions, as long as the smoothing window function is selected carefully. On the other hand, the smoothing technique in Equation 43 may not be enough if the input signal is also corrupted by noise, or has some problems in terms of frequency components and synchronization. The corruption of the input signal may occur when there is any unexpected problem in the electronics hardware or frequency analyzer to generate the input signal. Also, the results of the system identification may be severely degraded, if the input signal does not have enough frequency components and/or the application of each input signal is not exactly synchronized with the system period or sampling time of the DSP system. As evident from Equation 41, we should consider the frequency range of  $U(j\omega - jk\omega_p)$ , the shifted Fourier transform of the input signal, as well as  $U(j\omega)$ , in order to estimate the HTFs with good precision. If the input signal does not have enough frequency components,  $U(j\omega - jk\omega_p)$  may have very low magnitude in the bandwidth of interest, while  $U(j\omega)$  has reasonable magnitude, so that the estimate of the  $k$ th HTF  $G_k$  may be very inaccurate.

In order to reduce the effect of the inaccuracy in the input signal on the system identification performance, we devised another smoothing technique, in which some small penalty is added to the power spectral density of the input signal  $\hat{\Phi}_{UU}$  before inverting the matrix. In other words,

$$\hat{\mathbf{G}} = (\hat{\Phi}_{UU} + \varepsilon \mathbf{I})^{-1} \hat{\Phi}_{UY} \quad (44)$$

Here,  $\mathbf{I}$  is an identity matrix compatible with  $\hat{\Phi}_{UU}$ , and  $\varepsilon$  is a constant. This smoothing process reduces the magnitudes of the HTF a little bit, but reduces noise in the HTFs quite significantly. The role of the small penalty  $\varepsilon$  is to make the estimate of the transfer functions robust to the error or inaccuracy in the input signal.

As will be shown in the next section, noise in the input/output signal corrupts the estimate of the transfer functions quite significantly, and makes it difficult to distinguish between the HTFs with negligible magnitude but much noise, and those with much magnitude but significant variations. However, we can distinguish them easily using these smoothing processes in Equation 43 and 44. That is, HTFs insensitive to the window function  $w(\omega)$  and/or small penalty  $\varepsilon$  are real, while those sensitive to the smoothing process are artifact.

When employing the second approach to estimate HTFs, it should be pointed out that the output measurement due to each input must be obtained by allowing the response to settle down significantly before the next input signal is initiated. In that case, it can be reasonably assumed that  $Y_0$  is due to the first input,  $Y_1$  due to the second input, and so on.

In contrast to the first method, the second method doesn't require much computer memory or intensive computation work, because we can compute the transfer functions at each frequency independently, without considering the whole frequency response simultaneously. On the other hand, in the first method, we should generate several 'big' matrices, which cause much memory and long computation time, because the ad-hoc manner in the first method requires that we should take into account the power spectral density and cross-spectral density matrix of input and output spectrum with all frequencies simultaneously.

### B.3 Validation of System Identification Methods

Once we have developed the methodologies to identify LTP systems, it is important to validate our identification schemes before applying them to actual systems. For this reason, we selected a simple LTP system model, a Mathieu equation, whose harmonic transfer functions can be found analytically, and verified the accuracy of our schemes using the model. We first analyze the model by computing their HTFs analytically. Then, we apply our identification schemes to estimate the HTFs of the model using the designed input data and simulated output data, and assuming that the model is given as a 'blackbox'. Finally, we compare the analytic solutions with the results obtained using our identification schemes.

#### *Theoretical Analysis*

The Mathieu Equation is a well-known equation representing an LTP system. The canonical form of the lossy Mathieu equation that we employed for our analysis is

$$\ddot{x}(t) + 2\xi\omega_n\dot{x}(t) + (1 + 2\beta\cos\omega_p t)\omega_n^2 x(t) = 0 \quad (45)$$

Note that the parameter  $\beta$  in the equation determines the importance of the periodic effects. That is, the system is essentially LTI for small  $\beta$ , while the periodic effects are significant for large  $\beta$ .

In state-space, the system matrices are

$$\mathbf{A}(t) = \begin{bmatrix} 0 & 1 \\ -(1 + 2\beta\cos\omega_p t)\omega_n^2 & -2\xi\omega_n \end{bmatrix}, \mathbf{B}(t) = \begin{bmatrix} 0 \\ 1 \end{bmatrix}, \mathbf{C}(t) = [1 \quad 1] \quad (46)$$

The harmonics of the dynamics matrix,  $\mathbf{A}(t)$ , are

$$\mathbf{A}_0 = \begin{bmatrix} 0 & 1 \\ -\omega_n^2 & -2\xi\omega_n \end{bmatrix}, \mathbf{A}_1 = \mathbf{A}_{-1} = \begin{bmatrix} 0 & 0 \\ -\beta\omega_n^2 & 0 \end{bmatrix} \quad (47)$$

Since there are no periodic elements in  $\mathbf{B}(t)$  and  $\mathbf{C}(t)$  matrices,  $\mathbf{B}_0$  and  $\mathbf{C}_0$  are the same as the matrices  $\mathbf{B}(t)$  and  $\mathbf{C}(t)$  given in Equations 46, while all the higher harmonics are zero. Using Equation 11, we can calculate the HTFs of the Mathieu equation. Figure 15 shows four HTFs of the Mathieu equation. Other HTFs have negligible magnitude, so they are not shown in Figure 15. The system parameters used in the simulation are  $\beta=0.3$ ,  $\xi=0.01$ ,  $\omega_n=20\pi$  rad/sec (10 Hz), and  $\omega_p=80\pi$  rad/sec (40 Hz).

The HTFs shown in Figure 15 show the importance of LTP system analysis and identification. If the required bandwidth for this system is below 20 Hz, we can assume this system is LTI with the transfer function  $G_0$ , and apply various LTI control design methods to achieve the performance requirement, because  $G_0$  has much higher magnitude than other transfer functions at least by 20 dB below 20 Hz. However, if the bandwidth of interest is higher than 20 Hz, the LTI assumption does not hold, and we should analyze and design this system as LTP systems, because other transfer functions, such as  $G_1$  and  $G_{-1}$ , have similar or even higher magnitude than  $G_0$ .

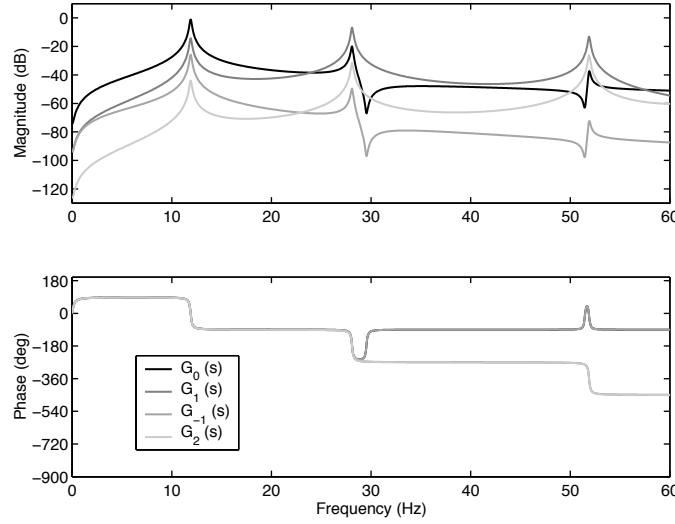


**Figure 15: Frequency responses of the lossy Mathieu equation.**

### ***Empirical Analysis***

After we analyzed the Mathieu equation model analytically, we used our identification algorithms to estimate the HTFs of the system. In order to evaluate the identification methods thoroughly and make the system identification procedure look more realistic, we considered three different cases. In the first case, we assume that both the input signal and output measurement are perfect, and there is no noise at all. By doing that, we can make sure that the LTP system can be actually identified using our algorithms, and we can analyze the effects of design parameters on the accuracy of the algorithms. On the other hand, we assume that the output measurement is corrupted by noise in the second case. We artificially generate the white noise, and add it to the output signal of the Mathieu equation. In the third case, the input signal as well as the output signal are assumed to be corrupted by noise. We used the actual input signal employed used to estimate the HTFs of a helicopter rotor during the wind tunnel test at Langley. By using these artificial noise in input and/or output signal, combined with the model, we can see whether our algorithms can be used to identify the actual physical systems. The following sections present the results of the analysis for these three cases.

#### **(1) Perfect Measurement and Perfect Input Signal**

First, it was assumed that both the input and output signal are perfect, and the two identification algorithms were used to estimate the HTFs of the Mathieu equation. In order to apply the algorithms successfully, especially the second method, the input signal should be designed carefully. Considering that we want to estimate four HTFs in this example, we need to use at least four chirp signals to estimate HTFs with good precision. In this example, we chose five chirp signals, each of which lasts 10 seconds and sweeps sine waves from 0 to 200 Hz. Each chirp in the input sequence differed in phase, by equal amounts over a period. Since we use five chirps, the phase difference between two consecutive signals is  $2\pi/5$ . We also add enough zero input to each chirp signal, while taking into account the relative phase, to allow the response to decay enough before the next input signal is initiated.

Figure 16 shows the input signals designed for this example, and the resulting output response of the system. The same parameters as in Section B.3 were used to simulate the Mathieu equation model. As expected, the output response corresponding to each of the chirp signals, which differ only in phase, is slightly different in magnitude.

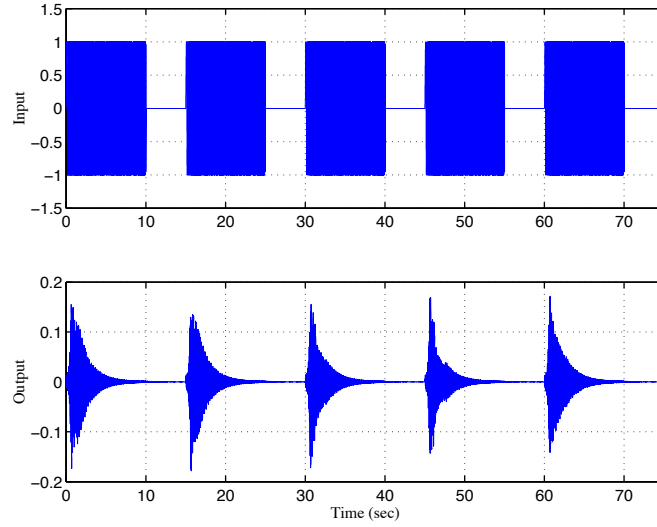


**Figure 16: Simulated input signals and corresponding response of the Mathieu equation.**

We now apply our identification schemes to the input and output response in Figure 16, to estimate four HTFs. Figure 17(a) and (b) show the HTFs of the Mathieu equation model estimated using the first and the second method, respectively, along with the analytic transfer functions. When applying the first method, the input signal in Figure 16 was treated as one long input signal, and the least square technique was applied to yield a well-defined identification problem. Also, the fourth difference operator was used to smooth the responses, and various values of the weighting factor  $\alpha$  were tested to investigate the effect of  $\alpha$  on the identification results and find a value resulting in the acceptable accuracy in the transfer functions. The result in Figure 17(a) corresponds to  $\alpha=100$ , but we found that the results of the first identification scheme are quite insensitive to  $\alpha$ . That is, the transfer functions remain almost unchanged when  $\alpha$  varies from  $10^{-7}$  to  $10^8$ .

On the other hand, the second method treats the five chirps in Figure 16 as five different inputs with different phase, and computes HTFs by inverting directly the power spectral density of the input spectrum. The HTFs in Figure 17(b) were obtained using Equation 43, i.e., without using any smoothing scheme, because it was assumed that there is no noise in the input and measurement signal. Also, we could use only five chirps in the input signal and estimate four HTFs quite successfully, but we should consider in general as many chirp signals as possible to improve the accuracy of the identification algorithms.

Figure 17(a)-(b) show that the analytic transfer function matches well with estimated transfer functions. The discrepancies between analytic and estimated transfer functions are so small that their effect will be negligible.

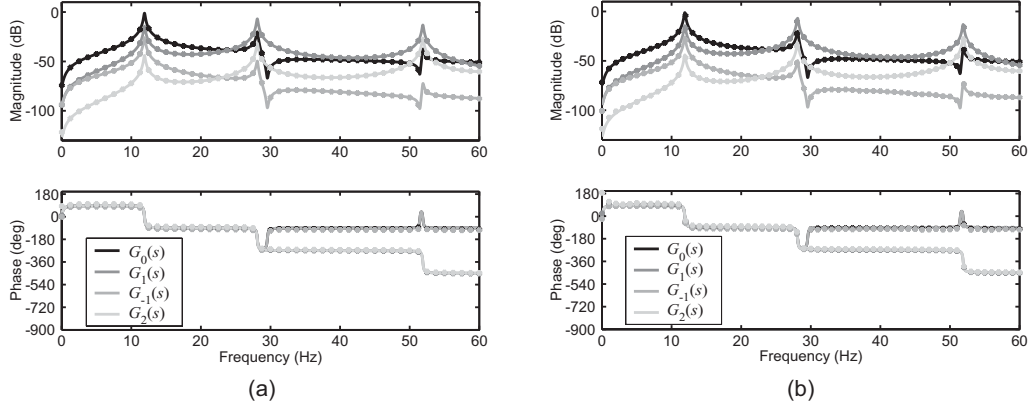


**Figure 17: Estimated harmonic transfer functions of the Mathieu equation system obtained using (a) the first method, (b) the second method. Solid and dotted line corresponds to analytical and empirical response, respectively.**

## (2) Imperfect Measurement and Perfect Input Signal

In the second case, we assumed that the output measurement is corrupted by noise, while the input signal is carefully designed and noiseless. In order to mimic the noisy measurement, we artificially generated the white noise, and added it to the output signal of the Mathieu equation. The main motivation of this section is to investigate the effects of the sensor noise on the performance of our identification schemes, and figure out how the design parameters can reduce the noise effect.

Figure 18 shows the input signal designed for this example, which is the same as that in the previous section, and the resulting output response with the noise. By comparing with the results in Figure 16, we can see clearly that the output response in Figure 18 is severely corrupted with the noise. The two LTP system identification methods were then applied to the input signal and output response in Figure 18. Ten input and output signals were averaged in the frequency domain using the cross- and power spectrum, to reduce the effects of the measurement noise. The results of applying the first identification method are shown in Figure 19, with various weight factors. The figure shows clearly the effect of the weighting factor on the estimate of HTFs, when they are corrupted with noise. It is evident from the figure that a high weighting factor smooths out the HTFs, by the sacrificing rapid variations with frequency or overestimating the system damping. When  $\alpha \leq 10^8$  (Figure 19(a)-(c)), there is little change in  $G_0(s)$  and  $G_1(s)$ , which have much higher magnitudes than other transfer functions. However, when  $\alpha = 10^9$  (Figure 19(d)), we can see that the transfer functions are too smoothed out, that is, the system damping is overestimated. This fact implies that we should use engineering judgment in selecting the weight factor, so that the transfer functions are smoothed enough, while preserving their important features.

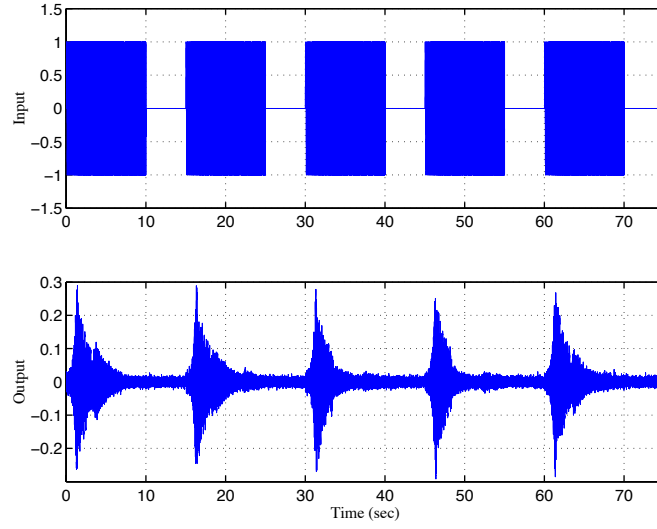


Figure 18: Simulated input signals and corresponding response of the Mathieu equation. The output is corrupted by white noise.

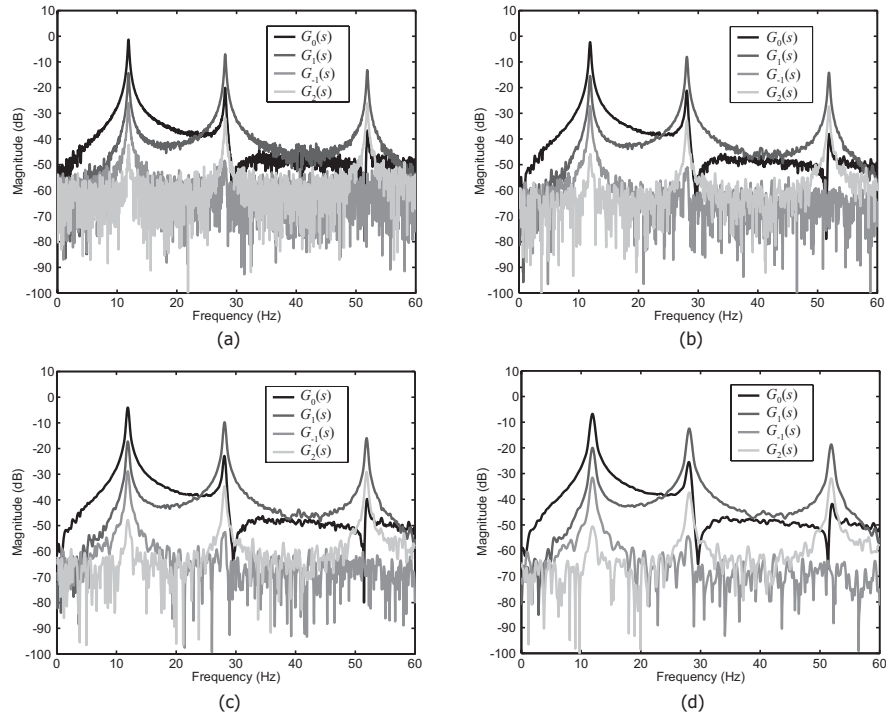
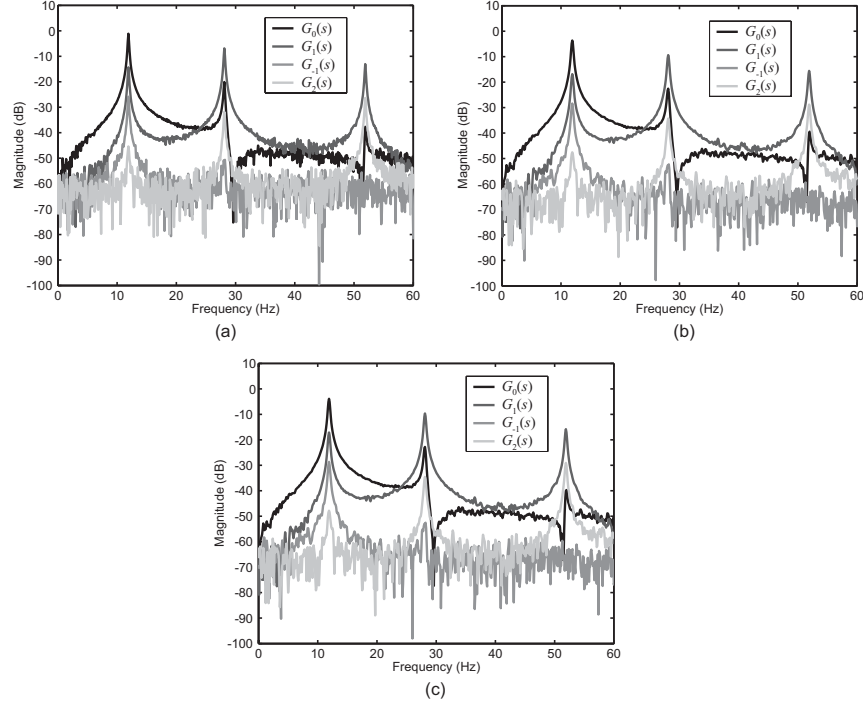


Figure 19: Harmonic transfer functions of the Mathieu equation system obtained using the first method with various  $\alpha$ . (a)  $\alpha=1$ , (b)  $\alpha=10^7$ , (c)  $\alpha=10^8$ , (d)  $\alpha=10^9$ .





**Figure 20: Harmonic transfer functions of the Mathieu equation system obtained using the second method. (a) Equation 40 (without smoothing technique). (b) Equation 43 (with the first smoothing technique). (c) Equation 44 (with the first and second smoothing techniques).**

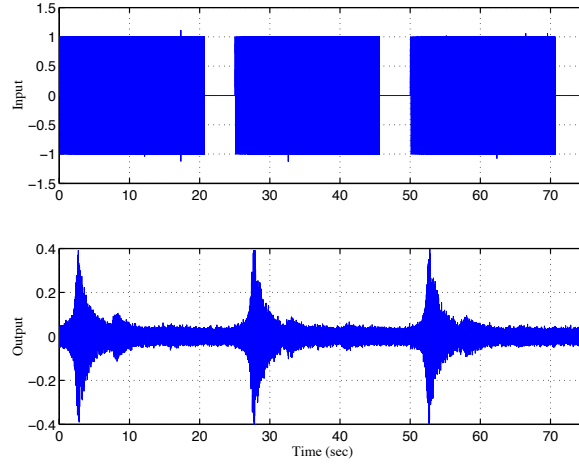
Figure 20 shows the results of using the second identification method to estimate the HTFs, without any smoothing (Figure 20(a)), with smoothing in Equation 43 (Figure 20(b)), and with smoothing in Equation 44 (Figure 20(c)). We can see that the smoothing technique in Equation 43 significantly reduces the effect of measurement noise, and improves the accuracy of the identification method. On the other hand, it is difficult to see the difference between the results in Figure 20(b) and Figure 20(c), that is, smoothing technique in Equation 43 and 44, because it is assumed that the input signal is well designed without any noise in this section. As mentioned earlier, the smoothing scheme in Equation 44 was devised to reduce the effect of any inaccuracy in the input signal on the performance of the identification method. The advantage of using the smoothing in Equation 44 will be evident in the next section.

### (3) Imperfect Measurement and Imperfect Input Signal

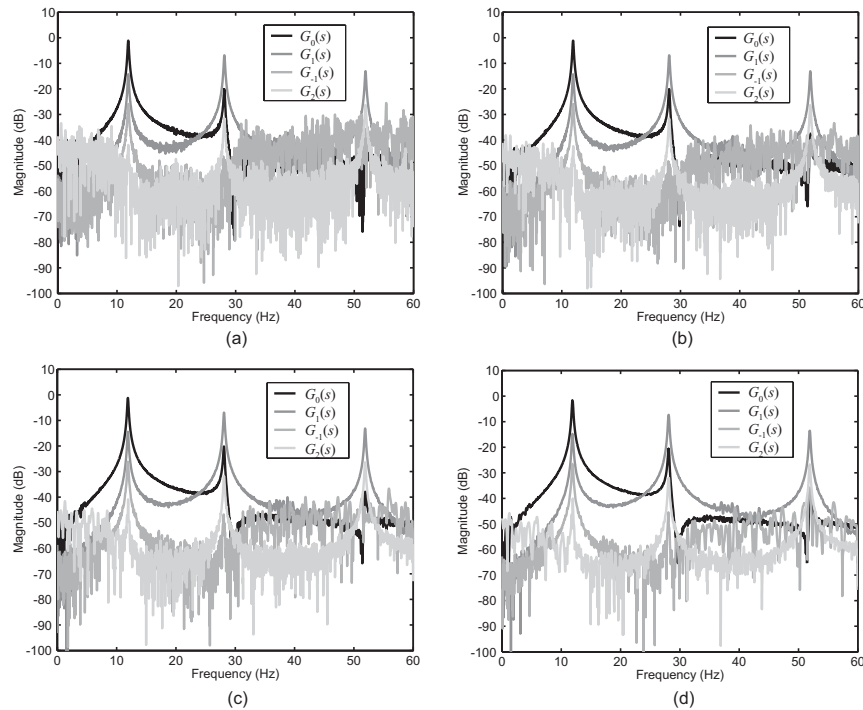
In the previous section, it was assumed that the measurement is noisy while the input signal is perfect, and the effects of the measurement noise on the performance of our identification schemes were investigated. In this section, we assume that the measurement is corrupted with noisy, and, in addition, the input signal is faulty, in that it is also noisy and does not have enough frequency components. We used the actual input signal used during the wind tunnel test at Langley to estimate the harmonic transfer functions of a helicopter rotor, which is linearly varying sine-sweep signal from 5 Hz to 70 Hz. The input signal, as well as the resulting output response of the Mathieu equation, are shown in Figure 21. Although not clear from the figure, the input signal is corrupted with several spikes, due to unexpected behavior of the experimental facility. As for the measurement noise, the same white noise used in the previous section was added to the output response of the Mathieu equation.

Figure 22 shows the results of applying the first identification method to the input and output response in Figure 21, with the same weights as in the previous section. Compared with the results in Figure 19, we can see that the effect of noise is more severe here but not much, and the smoothing with adequate weighting factor can effectively reduce it. On the other hand, the results in Figure 23, where the second identification method was applied, show that the effect of noise is much more significant if the

input signal is faulty, compared with the results in Figure 20. That is, in contrast to the first method, the second identification method is sensitive to the input signal. Also, the difference between the results in Figure 23(b) (smoothing technique in Equation 43) and Figure 23(c) (smoothing technique in Equation 44) is now apparent, which was not in the previous section. By using the smoothing in Equation 44, as well as in Equation 43, we can reduce considerably the effect of inaccuracy in the input signal on the performance of the second method. Therefore, we should be very careful in designing the input signal for the second method and use the smoothing methods in Equation 43 and, especially Equation 44, to make the method more robust to unexpected problems in the input signal.



**Figure 21: Input signal intentionally designed faulty, and corresponding response of the Mathieu equation. Both input and output signal are corrupted with noise.**



**Figure 22: Harmonic transfer functions of the Mathieu equation system obtained using the first method with various  $\alpha$ . (a)  $\alpha=1$ , (b)  $\alpha=10^7$ , (c)  $\alpha=10^8$ , (d)  $\alpha=10^9$ .**

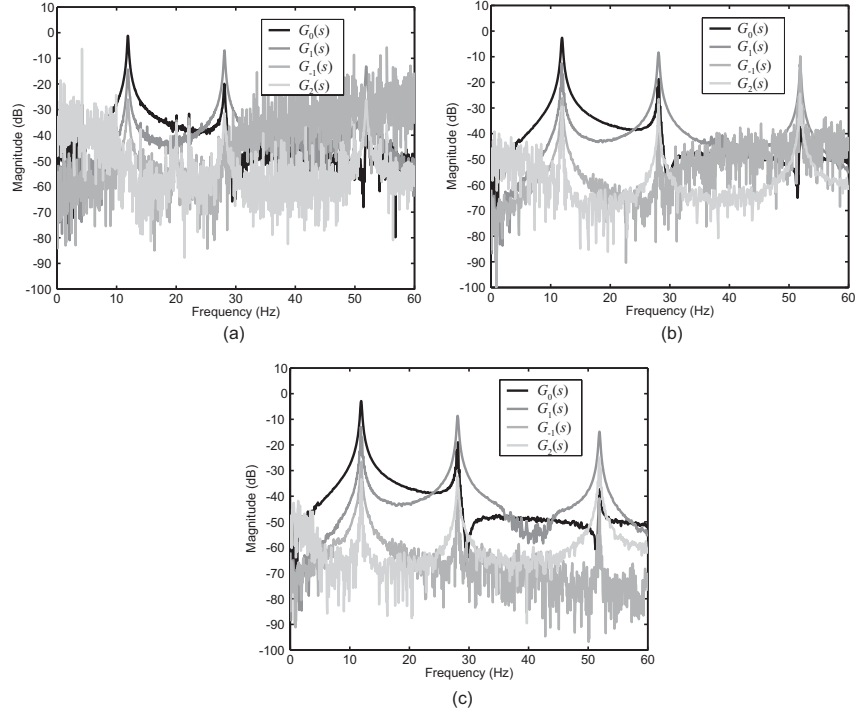


**Figure 23: Harmonic transfer functions of the Mathieu equation system obtained using the second method. (a) Equation 40 (without smoothing technique). (b) Equation 43 (with the first smoothing technique). (c) Equation 44 (with the first and second smoothing techniques).**

## C Summary of Wind Tunnel Test at Langley

While Boeing prepared for the flight test, we collaborated with Prof. Carlos Cesnik's research group at University of Michigan to support his NASA-supported program for the Active Twist Rotor (ATR) in forward flight in the Transonic Dynamics Tunnel (TDT) at NASA Langley. Figure 24 shows the ATR system mounted on the Aeroelastic Rotor Experimental System (ARES) helicopter testbed with in the TDT.



**Figure 24: ATR system mounted on the ARES helicopter testbed with in the TDT.**

The collaboration was carried out to test our system identification methodology and continuous-time higher harmonic control (HHC) algorithms on actual rotor. For the wind tunnel test, we implemented the system identification algorithms in Simulink to estimate the transfer function of the rotor, and designed

continuous-time HHC algorithms incorporating an anti-windup scheme. We also transferred our system identification and HHC design technology to Prof. Cesnik's group to support the wind tunnel test for the ATR at NASA Langley. This section summarizes the results of the flight test at Langley.

### C.1 System Identification of Rotor Systems

We applied our identification schemes described in Section B to the ATR, which consists of a fully articulated four blades incorporating active materials as actuators. We estimated the transfer functions of the ATR system at various advance ratio ( $\mu=0.14, 0.2, 0.267, 0.333$ ), by applying electric field to the active materials made of Active Fiber Composite (AFC) packs in each ATR blade, and measuring the system output from a force sensor mounted inside the helicopter hub. In order to estimate the HTFs of the ATR system using our identification schemes, we carefully designed the input signal to excite the system and measure the output response, considering the system period,  $T=2\pi/\omega_p$ , and the number of HTFs to be identified,  $n_h$ . We used a linearly varying sine-sweep signal from 5 Hz to 70 Hz for each chirp input, since the main frequency of interest in our experiment is 4 /rev, which is approximately 46 Hz. The whole input signal consists of 20 chirp signals, each of which lasts 20 seconds and has equally-spaced relative phase. We used 20 chirp signals, which may appear more than adequate in this case, in order to improve the accuracy of the identification algorithms. It should be noted that considering more chirps in the input signal achieves better identification results. Therefore, it becomes more critical to consider as many chirps as possible when applying the algorithms to actual systems, because the measurement output may be seriously corrupted by sensor noise in a real world. Figure 25 shows some parts of the input signal and the corresponding response of the ATR system.

Before applying our identification schemes to estimate the HTFs of the rotor system (collective, sine cyclic, cosine cyclic) at various advance ratios, we selected one specific case, i.e., collective transfer function at  $\mu=0.333$ , and tested our two system ID methods in detail. We followed the same procedure in Section B.3, in order to see whether our methods yield the physically meaningful results. In the first method, we treated the input signal consisting of 20 chirps as one long input signal, and employed the least square technique to yield a well-posed identification problem. Since there is no decisive way of determining the optimal value of the weighting factor  $\alpha$ , we began with  $\alpha=10^3$  and increased the value exponentially to find a reasonable value achieving the acceptable accuracy. Figure 26(a)-(d) show the five collective HTFs at  $\mu=0.333$ , which were obtained using the first method with  $\alpha=10^6, 10^9, 10^{12}$ , and  $10^{15}$ , respectively. The case for  $\alpha=10^3$  was not shown here, because the resulting transfer functions were too noisy.

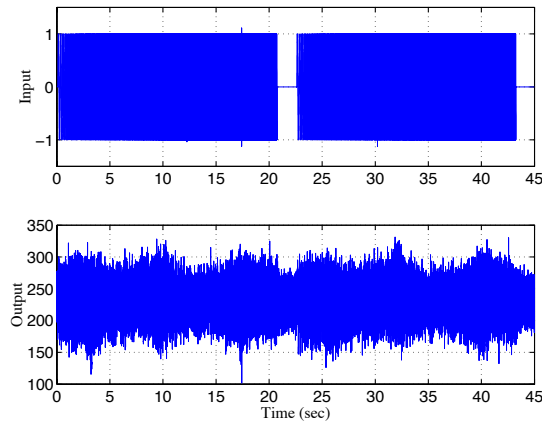


**Figure 25: Designed input signal and corresponding response of the ATR system.**

Figure 26 shows clearly the effect of the weighting factor on the HTFs. It is evident from the figure that a high weighting factor smoothes out the HTFs, while sacrificing the rapid variations with frequency

in them. Since it is often difficult to figure out whether the rapid variation is due to the noise or exists physically, we should test various values of the weighting factor and compare their results. We can also observe from Figure 26 that there exist HTFs quite insensitive to the weighting factor. That is, we can see that  $G_0(s)$ ,  $G_1(s)$ , and  $G_2(s)$  do not change much when we vary the weighting factor  $\alpha$  from  $10^6$  to  $10^{15}$ , while  $G_{-2}(s)$  and  $G_{-1}(s)$  change significantly depending on  $\alpha$ . When  $\alpha=10^6$ , the magnitude of  $G_{-2}(s)$  and  $G_{-1}(s)$  is similar to, or even higher than, that of the other three HTFs, but  $G_{-2}(s)$  and  $G_{-1}(s)$  become negligible as  $\alpha$  increases. What this fact may imply is that  $G_0(s)$ ,  $G_1(s)$ , and  $G_2(s)$  (which do not depend much on  $\alpha$ ) are the transfer functions that actually exist in the system, while  $G_{-2}(s)$  and  $G_{-1}(s)$  (which are very sensitive to  $\alpha$ ) do not exist physically, or have so low magnitudes that they cannot be identified or can be neglected.

In contrast to the first method, the second method treats the 20 chirps (some of them are shown in Figure 25) as 20 different inputs with different phase, and measures 20 different output response to estimate HTFs. Figure 27(a) shows the five HTFs obtained using Equation 40, that is, without using any smoothing scheme. Figure 27(b) shows the five HTFs obtained using the smoothing technique in Equation 43, while Figure 27(c) shows the same results using Equation 44. Figure 27 clearly indicates how the smoothing procedures affect the resulting HTFs estimated using the second method. It can be observed from the figure that the smoothing procedures in the second method reduce the noise in the HTFs significantly, and enable us to distinguish between the HTFs with negligible magnitude but much noise, and those with much magnitude but significant variations. Figure 27 shows that the use of the smoothing procedures make little differences in  $G_0(s)$ ,  $G_1(s)$ , and  $G_2(s)$ , while there is significant change in  $G_{-2}(s)$  and  $G_{-1}(s)$  depending on the window function and the penalty  $\epsilon$ . This observation implies that HTFs insensitive to the smoothing exist actually in the system, while those sensitive to smoothing may be an artifact of inaccurate measurement. It should be also noted that we could draw the same conclusions using the first method.

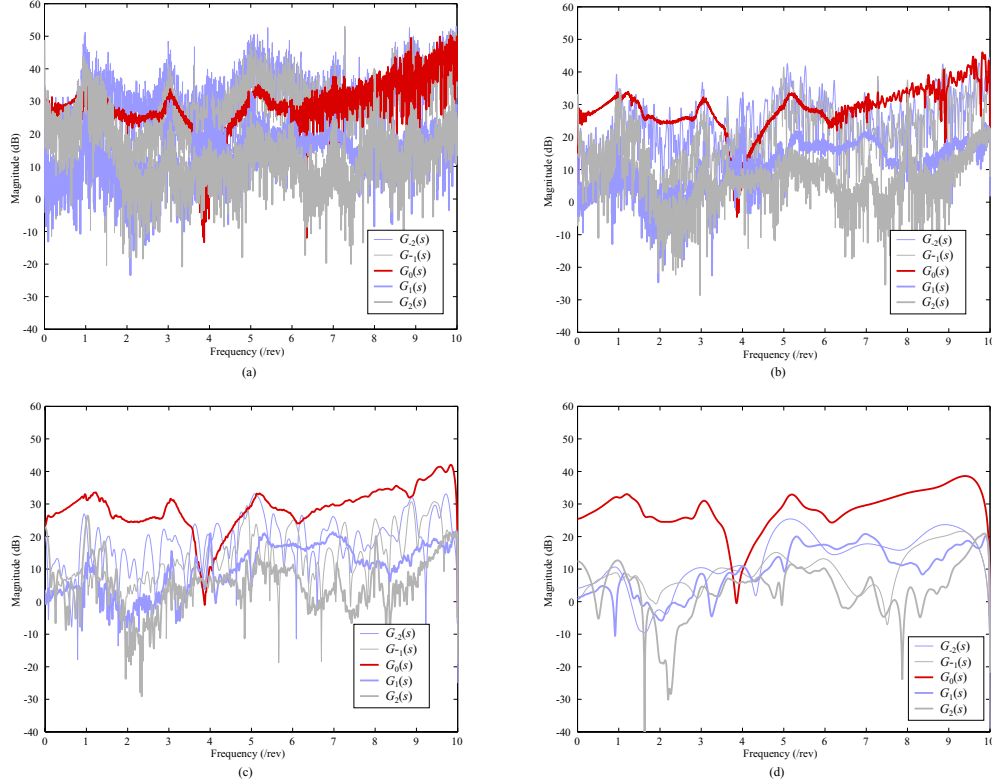


**Figure 26: Harmonic transfer functions of the ATR system obtained using the first method with various  $\alpha$ . (a)  $\alpha = 10^6$ , (b)  $\alpha = 10^9$ , (c)  $\alpha = 10^{12}$ , (d)  $\alpha = 10^{15}$ .**

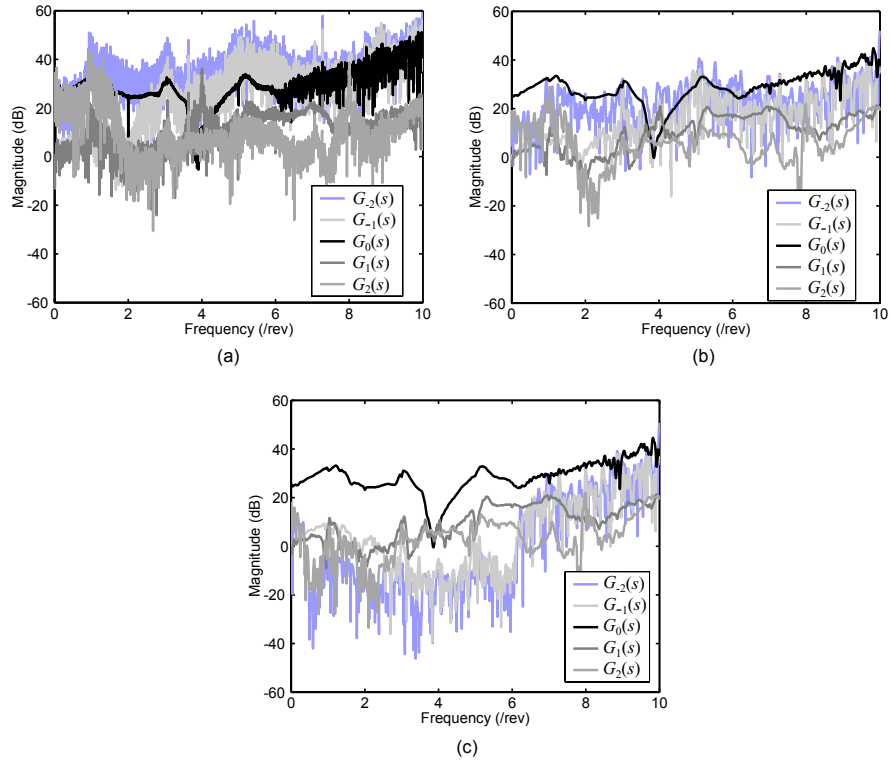


**Figure 27: Harmonic transfer functions of the ATR system obtained using the second method. (a) Without smoothing procedure. (b) With smoothing procedure.**

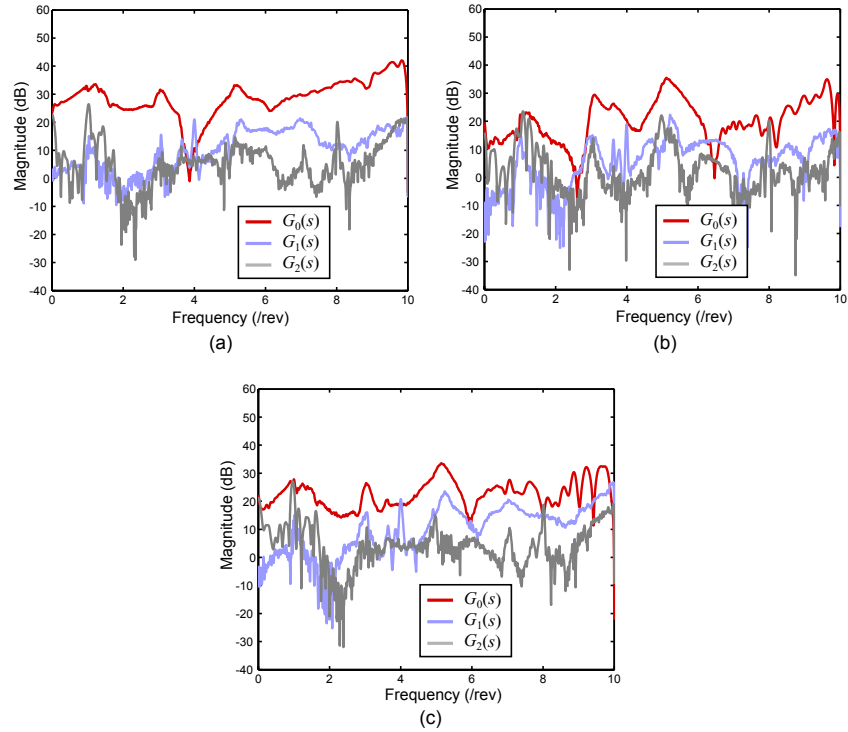


**Figure 28: Harmonic transfer functions of the ATR system. (a) Collective, (b) Cosine cyclic, (c) Sine cyclic.**

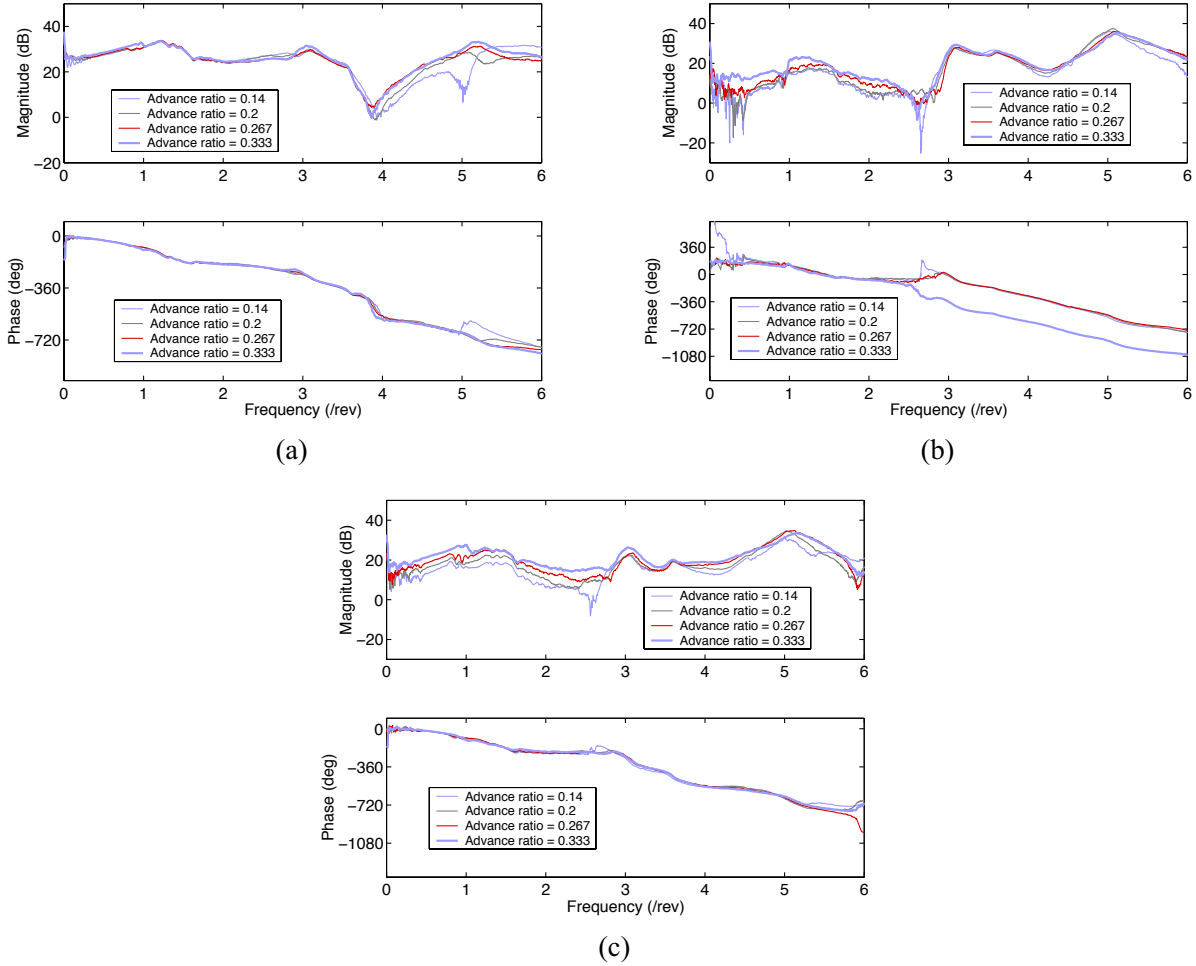


**Figure 29: Effect of advance ratio on the HTFs of the ATR system. (a) Collective, (b) Cosine cyclic, (c) Sine cyclic.**

After we verified our identification algorithms in detail using one specific case (collective transfer function at  $\mu=0.333$ ), we applied the algorithms to estimate the HTFs of the ATR system (collective, cosine cyclic, and sine cyclic at  $\mu=0.14, 0.2, 0.267, 0.333$ ). Figure 28(a)-(c) show the three HTFs of the ATR system which we believe physically represent the system (i.e.,  $G_0(s)$ ,  $G_1(s)$ , and  $G_2(s)$ ) at  $\mu=0.333$ , for collective, cosine cyclic, and sine cyclic input, respectively. The results in Figure 28 show that the magnitude of  $G_0(s)$  (corresponding to LTI transfer function) is much larger than other two HTFs, at least by 20 dB. This result implies that we can achieve significant amount of vibration reduction using continuous-time controllers based on LTI plant assumption. This is important, in that it indicates that classical control laws should work well for the controlling the ATR rotor, which should greatly simplify the design of closed-loop controllers for the ATR rotor.

Figure 29(a)-(c) show the magnitude and phase of  $G_0(s)$  of the ATR system at  $\mu=0.14, 0.2, 0.267, 0.333$ , for collective, cosine cyclic, and sine cyclic input, respectively. The results in Figure 29 show that the dynamics of the ATR system behave as expected, in that the collective transfer functions are hardly affected by advance ratio, while the sine cyclic transfer functions are proportional to advance ratio, both in the low-frequency range. Also, the results indicate that the HTFs of the ATR system are not so sensitive to advance ratio, especially their phase, which implies that a controller carefully designed with fixed gains should work adequately for various values of advance ratio.



## C.2 Closed-loop Experimental Results

Based on the results of the system identification for the ATR system, we designed and implemented continuous-time higher harmonic control (HHC) algorithms to reduce the vibration of helicopters. We chose continuous-time controllers, rather than traditional discrete-time HHC algorithms developed in the early 1980's, because our previous research results show that continuous-time controllers yield better closed-loop performance than similar discrete-time controllers [4]. More importantly, the results show that the discrete-time controller, which implicitly assumes that the rotor response is quasisteady, can drive the rotor unstable.

Furthermore, we designed controllers based on the assumption that the rotor system is linear time invariant (LTI), considering that the magnitude of  $G_0(s)$  is much larger than other HTFs. That is, we assumed that the rotor system behaves as an LTI system with a transfer function  $G_0(s)$ , and we designed continuous-time controllers so that the loop transfer function (i.e.,  $G_0(s)$  times the controller transfer function) has a high magnitude at the target frequencies, while preserving enough gain and phase margins.

We tested our continuous-time HHC systems using various gain combinations for each control input (i.e., collective, cosine cyclic, and sine cyclic), and flight conditions ( $\mu=0.14, 0.2, 0.267, 0.333$ ). For most cases, we could reduce the vibration level significantly at the target frequencies (1P and 4P components were selected as target frequencies in this experiment). Table 1 summarizes the level of vibration reduction we could achieve for various closed-loop experiments conducted at Langley. Figure 30 shows the typical closed-loop performance obtained using our control systems, with ratios of open-loop response to closed-loop response. Note that negative and positive ratios indicate attenuation and amplification of the vibration, respectively. Figure 30 indicates that more than 30 dB of reduction can be achieved at both 1P and 4P components using our continuous-time HHC system.

This section briefly describes the results of closed-loop experiments conducted at Langley. For more information about the closed-loop results, refer to [5] (attached to this report).

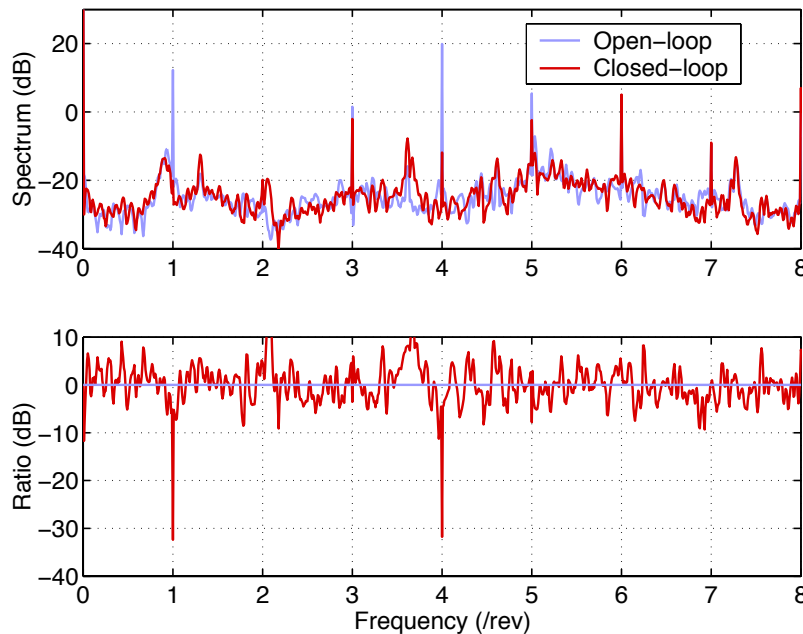


Figure 30: Typical open & closed-loop spectra of the hub normal shear vibratory load.



**Table 1: Results of vibration reduction for ATR system (cited from [5])**

Case Name	Open-loop RMS normal load (lb)	Closed-loop RMS normal load (lb)	Performance (Reduction level, dB)
Cyc1	22.35	13.77	4.2
Cyc2	22.45	15.14	3.4
Cyc3	22.52	12.06	5.4
Cyc4	22.55	8.87	8.1
Cyc5	22.61	7.19	10.0
CollCyc1	22.60	12.21	5.3
CollCyc2	22.50	8.75	8.2
CollCyc3	22.26	7.60	9.3
CollCyc4	10.71	0.03	51.1
CollCyc5	10.63	0.04	48.5
CollCyc6	14.06	1.41	20.0
CollCyc7	14.01	0.36	31.8
CollCyc8	21.45	10.15	6.5
CollCyc9	21.35	8.72	7.8